

Extremals of Log Sobolev inequality on non-compact manifolds and Ricci soliton structures

*Original*

Extremals of Log Sobolev inequality on non-compact manifolds and Ricci soliton structures / Rimoldi, M., Veronelli, G.. - In: CALCULUS OF VARIATIONS AND PARTIAL DIFFERENTIAL EQUATIONS. - ISSN 0944-2669. - 58:2, Art. 66(2019), pp. 1-26. [10.1007/s00526-019-1518-z]

*Availability:*

This version is available at: 11583/2728324 since: 2020-02-03T23:33:29Z

*Publisher:*

Springer

*Published*

DOI:10.1007/s00526-019-1518-z

*Terms of use:*

This article is made available under terms and conditions as specified in the corresponding bibliographic description in the repository

*Publisher copyright*

Springer postprint/Author's Accepted Manuscript

This version of the article has been accepted for publication, after peer review (when applicable) and is subject to Springer Nature's AM terms of use, but is not the Version of Record and does not reflect post-acceptance improvements, or any corrections. The Version of Record is available online at: <http://dx.doi.org/10.1007/s00526-019-1518-z>

(Article begins on next page)



## Ti<sub>3</sub>C<sub>2</sub>T<sub>x</sub> MXenes in Lithium-Sulphur batteries to balance polysulphide adsorption and Li<sub>2</sub>S deposition

Leonardo Alberto Luciano<sup>a</sup>, Tiziano Di Giulio<sup>c</sup>, Francesco Pellegrino<sup>b</sup>, Roberto Colombo<sup>a</sup>, Elisabetta Mazzotta<sup>c</sup>, Cosimino Malitesta<sup>c</sup>, Valter Maurino<sup>b</sup>, Julia Amici<sup>a</sup>, Marco Minella<sup>b</sup>, Daniele Versaci<sup>a,\*</sup>

<sup>a</sup> Electrochemistry Group, Department of Applied Science and Technology (DISAT), Politecnico di Torino, C.so Duca degli Abruzzi 24, Torino 10129, Italy

<sup>b</sup> Department of Chemistry, Università di Torino, Via Pietro Giuria 7, Torino 10125 Italy

<sup>c</sup> Laboratory of Analytical Chemistry, Department of Biological and Environmental Sciences and Technologies (Di.S.Te.B.A.), Università del Salento, Via Monteroni, Lecce 73100 Italy

### ARTICLE INFO

#### Keywords:

Lithium-sulphur batteries  
MXenes  
Cathode  
Polysulphides  
Etching conditions

### ABSTRACT

Lithium-Sulphur (Li-S) batteries are a promising post-lithium-ion energy storage technology due to sulphur high theoretical capacity, low toxicity and natural abundance. Nevertheless, sulphur multistep reduction reactions involve the formation of soluble lithium polysulphides, whose uncontrolled migration to the anode (*shuttle effect*) and sluggish conversion kinetics lead to capacity fading and poor cycling stability. To overcome these issues, different materials capable of binding polysulphide species, catalysing their conversion and controlling Li<sub>2</sub>S deposition have been explored as sulphur hosts. In this context, MXenes have recently emerged owing to their good electrical conductivity and polar surface chemistry.

The present work aimed at studying Ti<sub>3</sub>C<sub>2</sub>T<sub>x</sub> MXenes as sulphur hosts for Li-S batteries. In particular, four samples of 2D titanium carbide were prepared by varying temperature, time and concentration of the classic synthesis involving the use of hydrogen fluoride. The synthesised Ti<sub>3</sub>C<sub>2</sub>T<sub>x</sub> were characterised using physico-chemical and electrochemical techniques to evaluate their affinity to polysulphide species and their potential activity as catalysts for sulphur redox reactions. The results show that slight changes in the synthesis conditions influence the balance between polysulphides adsorption and electrochemical conversion. In particular, combining lower acid concentration and longer reaction time leads to MXenes with improved overall electrochemical behaviour, delivering stable cycling up to 500 cycles with improved Coulombic Efficiency (>99%) and capacity retention (>70%), with a capacity loss < 0.30% per cycle at C/5. Although MXenes exhibit lower porosity and electrical conductivity than conventional carbon hosts, the present study highlights their effectiveness in suppressing the *shuttle effect* and control Li<sub>2</sub>S deposition.

### 1. Introduction

Lithium-ion batteries (LIBs) are currently the most widely used and consolidated technology for both energy storage and transport electrification. However, nowadays on the market LIBs are approaching their theoretical limits in terms of energy density and specific capacity and face several disadvantages, such as supply constraints on raw materials and high production costs, which limit their ability to fully meet the growing demand for energy storage solutions. Consequently, the study and development of alternative technologies, the so-called post-lithium-ion systems, is of crucial importance to make them commercially viable

in the future and able to compete with LIBs. Among these systems, Lithium-Sulphur batteries (Li-S) are among the most interesting and promising technologies [1]

Sulphur is an abundant, low-cost, and non-toxic element [2] and with a specific theoretical capacity of 1672 mAh g<sup>-1</sup>, which is an order of magnitude higher than intercalation materials commonly used in LIBs (i. e. lithium iron phosphate, lithium nickel manganese cobalt oxide) [3] This is due to the different electrochemical mechanism occurring in the cell, which is based on conversion reactions instead of lithium ion insertion typical of LIBs. As a consequence, lithium-sulphur batteries can potentially reach theoretical energy densities up to five times the value

\* Corresponding author.

E-mail address: [daniele.versaci@polito.it](mailto:daniele.versaci@polito.it) (D. Versaci).

<https://doi.org/10.1016/j.cej.2026.101260>

Available online 20 May 2026

2666-8211/© 2026 The Authors. Published by Elsevier B.V. This is an open access article under the CC BY-NC-ND license (<http://creativecommons.org/licenses/by-nc-nd/4.0/>).

of lithium-ion technology, permitting them to be manufactured in lighter and more compact cell designs. Unfortunately, some issues still limit their practical application [4].

As sulphur complete reduction involves multiple electrons, the mechanism is complex and based on the so-called Sulphur Reduction Reactions (SRR) in which lithium polysulphides (LiPS) are formed. First,  $S_8$  molecules are reduced to long-chain LiPS ( $Li_2S_8$  and  $Li_2S_6$ ) and then to short-chain polysulphides  $Li_2S_4$ , accounting for the 25% of theoretical specific capacity. All these species are soluble in the commonly employed ether-based electrolyte and their solubilisation and consequent diffusion give rise to the *shuttle effect* [5] Because of this, long-chain LiPS can reach the anode and react with metallic lithium, passivating its surface; moreover short-chain LiPS can diffuse back to the cathode during the charging process of the cell. As a result, part of the active material is lost during cycling and side reactions occur, limiting cell performance, cycling life and Coulombic Efficiency (C.E.) [6] Short-chain polysulphides are reduced at the cathodic interface to  $Li_2S_2$  and  $Li_2S$  species, which are insoluble and precipitate, passivating the electrode surface because of their insulating nature. This reaction should account for the remaining 75% of the theoretical specific capacity. Due to the above-mentioned problems, only a fraction of the sulphur present in the cathode is practically available [7] Another important issue is the great change in volume (approximately 80%) of the cathodic active material during cycling due to the density differences among  $S_8$  and  $Li_2S$ , which could lead to the collapse of the electrode structure. During the charge, the described process occurs in the opposite direction, with the solubilization of lithium sulphide and the reprecipitation of sulphur after LiPS oxidation, while  $Li^+$  ions go back to the anode, where they are deposited as metallic lithium [8]

To overcome the presented challenges, many different types of conductive materials able to confine sulphur, interact with LiPS and catalyse their electrochemical reactions as well as contain volume contractions and expansions, have been studied as sulphur hosts such as carbons, transition metals, metallic compounds, polymers, metal-organic and covalent-organic frameworks (MOFs and COFs) and 2D materials [9–18]

Among 2D materials, MXenes have taken on an increasingly prominent role in recent years due to their broad range of applications [19] They are a wide class of transition metal carbides and nitrides with a bidimensional structure and general formula  $M_{n+1}X_n$ , where M stands for an early transition metal, X represents carbon or nitrogen and  $n$  is a number between 1 and 3 [20] They can be obtained from their relative MAX phase, a tertiary carbide or nitride with general formula  $M_{n+1}AX_n$  (A is usually aluminium or another element from group III or IV) and a lamellar structure, by simply removing the layers of the A element and separating the resulting bidimensional planes. In the case of Ti-based MXenes, the simplest route to remove aluminium is chemical etching of the A-type atoms using hydrofluoric acid (HF) [21] During the etching process, several unsaturated M atoms are generated and react with molecules in the surrounding media, forming surface functional groups, often expressed as “ $T_x$ ”, that depend on solvents and reagents used in the synthesis, influencing the properties of the final material. Alternatively, the obtained materials can be further processed, tailoring their surface chemistry to satisfy the needs of each specific application, but increasing the complexity and the cost of their production and purification steps [22]

Despite their recent discovery, MXenes and their applications in Li-S have been widely studied, especially as bidimensional titanium carbide in the form of  $Ti_2C$  and  $Ti_3C_2$ . Nazar group was the first to apply  $Ti_2CT_x$  [23] and  $Ti_3C_2T_x$  [24] MXenes in the cathodic formulation of Li-S, studying their interaction mechanism with polysulphide species due to the presence of surface hydroxyl groups and unsaturated titanium atoms. After sulphur reduction, long-chain polysulphides are adsorbed on the surface of MXenes particles, where they react with  $-OH$  groups, forming thiosulphate species  $S_2O_3^{2-}$ . These new species can further react with other LiPS, producing insoluble  $Li_2S_2$  or  $Li_2S$  and polythionate

species following the Wackenroder reaction mechanism [25] At the same time, unsaturated Ti atoms lack electrons and therefore behave as Lewis acids, chemically bonding negatively charged polysulphide species, which exhibit Lewis basic characteristics.

As mentioned above, MXenes and especially two-dimensional titanium carbide [26] have been widely studied for energy storage applications, including Li-S systems. Concerning their application in Li-S, various types of MXenes have been employed, adopting different strategies, taking advantage of their different physicochemical properties [27–29] At the cathode side [30], MXenes have been used as: pure sulphur hosts, exploiting their layered structures to accommodate the active material [31–33]; combined with carbonaceous materials like reduced graphene oxide [34], carbon nanotubes [35] and nanofibers [36] to obtain porous structures; as part of composite materials together with doped-carbons [37,38] or metallic compounds [39–43] to enhance affinity towards lithium polysulphides and regulate  $Li_2S$  deposition process. In addition, numerous MXenes compositions and different surface properties have been computationally investigated, although many of these materials have not been synthesised or experimentally tested yet.

MXenes have also been used to functionalise separators because of their strong adsorption of polysulphide species, preventing them from reaching the anode and reacting with it. This has been achieved by covering commercial polypropylene separators with delaminated or alkali-treated MXenes or even adding MXene-based interlayers between cathode and separator [44–46] Lastly, MXene-based materials have been used to produce lithiophilic anodic materials thanks to their electronegative fluorinated and oxygenated surface groups which can homogenise lithium deposition and prevent the formation of dendrites [47–49]

The main objective of the present work was to investigate how variations in the MAX phase etching process, such as acid concentration, reaction time and temperature, lead to  $Ti_3C_2T_x$  MXenes with different physicochemical and morphological properties. These differences not only affect the interaction with lithium polysulphides during charge and discharge processes, but also influence the interaction between MXene and sulphur during the melt diffusion process and the subsequent formation of the composite material. To the best of our knowledge, such a systematic investigation remains relatively unexplored in the current literature.

In fact, unlike most recent studies on MXenes, which are primarily focused on the development of complex heterostructures, hierarchical architectures, doped systems, or composite materials that are often difficult to scale up, the present work highlights that simple variations in the etching conditions are sufficient to modulate the electrochemical behaviour of the Li-S system [50–68]

The obtained materials were characterised with different physicochemical and electrochemical techniques and then used directly as sulphur hosts without any further processing. The sulphur cathodes obtained from the different MXene samples were characterised electrochemically through galvanostatic cycling at C/5 and compared. Finally, the material with the most promising electrochemical performance was tested in galvanostatic cycles for 500 cycles at C/5 to evaluate its medium-long-term behaviour.

## 2. Experimental section

### 2.1. Material preparation

#### 2.1.1. $Ti_3C_2$ MXenes synthesis

Four different samples of  $Ti_3C_2$  MXenes were obtained using hydrofluoric acid as aluminium etching agent and  $Ti_3AlC_2$  MAX phase (Sigma-Aldrich,  $\geq 90\%$ , particle size  $\leq 100 \mu m$ ) as precursor. The samples were named MX<sub>aa</sub>, where aa digits stand for the specific synthesis parameters used for each sample, as reported in Table 1. Specifically, for all samples, 1.5 g of MAX phase are weighted and transferred into a 200

**Table 1**  
Variable reaction conditions.

Sample	HF concentration (%)	Time (h)	Temperature ( °C)
MX_01	5	24	40
MX_02	10	48	60
MX_03	5	48	40
MX_04	10	24	60

ml Teflon® lined steel autoclave (DAB3, Berghof) 45 mL of hydrofluoric acid at the desired concentration (see Table 1), obtained by diluting a 48% solution (Sigma-Aldrich, ACS reagent), are cooled with an ice bath and added dropwise to the precursor under magnetic stirring. Then, the mixture is sealed, stirred at 500 rpm and heated with a 1 °C min<sup>-1</sup> slope to reach the temperature reported in Table 1, which is kept for the corresponding time. The heating/stirring was carried out with a heating mantle mounted on a magnetic stirrer/heater (MRHEI standard, Heidolph) and a temperature controller/programmer (BTC-3000, Berghof) equipped with a type K thermocouple.

After the synthesis, samples are transferred into Falcon® tubes and centrifuged for 5 min at 6500 rpm (Centrifuge ALC PK 131R) to separate MXene phase from the acid solution, which is eliminated. The solid fraction is, then, repeatedly washed and centrifuged for 20 min at 6500 rpm using Milli-Q® water until the solution pH reaches a value between 4 and 6. At this point, supernatant water is removed, samples are freeze-dried to obtain MXene powders and stored in a glovebox (Unilab MBraun) filled with an argon atmosphere (moisture and oxygen concentration below 0,5 ppm).

### 2.1.2. MXene/sulphur composites preparation

MXene/sulphur composites were prepared by mechanically mixing sulphur (Sigma-Aldrich, *purum p.a.*, ≥99.5%) with each Ti<sub>3</sub>C<sub>2</sub> sample (weight ratio 3:1) for 1 hour at 10 Hz in a ball miller (Retsch MM400) and then heating at 155 °C for 5 h in a muffle furnace using an Ar-filled sealed vial. After the thermal treatment, the composite was grounded and used as cathodic material for electrode preparation. Effective sulphur content of the as-obtained powder was determined by thermogravimetric analysis in air (TGA).

## 2.2. Materials characterisation

X-Ray Diffraction (XRD) analysis was carried out by a Malvern PANalytical Empyrean (Cu K $\alpha$  radiation) diffractometer. Data were collected with a 3D solid state detector (PIXcel) in 2 $\theta$  range of 5–65°

X-ray photoelectron spectroscopy (XPS) was performed using an AXIS ULTRA DLD spectrometer (Kratos Analytical) equipped with a monochromatic Al K $\alpha$  source ( $h\nu=1486.6$  eV), operated at 150 W (10 kV, 15 mA). The base pressure in the analysis chamber was maintained at  $\sim 5 \cdot 10^{-9}$  Torr. Survey spectra were acquired with a pass energy of 160 eV and a step size of 1.0 eV, while high-resolution spectra were collected at a pass energy of 20 eV with 0.1 eV step increments. The analyzed area was approximately 700  $\mu\text{m} \times 300 \mu\text{m}$ . Charge neutralization was provided using an electron flood gun. Data processing and peak fitting were carried out using CasaXPS (v.2.3.16). For quantitative analysis, peak areas were corrected using relative sensitivity factors (RSFs). For MXene (Ti<sub>3</sub>C<sub>2</sub>T<sub>x</sub>) samples, spectral processing followed established procedures found in the literature [69] MXene-related components were fitted using asymmetric line shapes to account for their conductive character, and a Tougaard background was applied to the Ti 2p region; for consistency, the same background was used for the C 1 s, O 1 s, and F 1 s spectra. Due to the presence of multiple overlapping components within broad envelopes, the full width at half maximum (FWHM) of Ti<sub>3</sub>C<sub>2</sub>T<sub>x</sub>-related components was constrained to be equal within the Ti 2p<sub>3/2</sub> group and, separately, within the Ti 2p<sub>1/2</sub> group, while allowing broader Ti 2p<sub>1/2</sub> peaks as expected from the Coster–Kronig effect. The binding energy scale was referenced to the Ti–C–Ti C 1 s peak at 282.0 eV, as BE of the C

atoms in the octahedral sites, Ti–C–Ti, is not affected by the type of surface terminations attached during etching in F-ion-containing acids, as widely reported for MXenes synthesised by etching in F-containing acids [70]

Field-Emission Scanning Electron Microscopy (FESEM) analysis was carried out by Zeiss SUPRA™ 40 with Gemini column and Schottky field emission tip (tungsten at 1800 K). Acquisitions were made at an acceleration voltage of 5 kV and working distance (WD) between 3.6 – 3.8 mm, with magnification up to 25k.

Particle size distribution statistics were derived from FESEM micrographs using a Python image analysis code developed and run on Spyder editor according to the methodologies for 2D materials and, in particular MXenes, reported in literature [71,72]

Thermogravimetric analysis (TGA) was carried out with a TA Instruments TGA Q500 by heating the samples from 25 to 800 °C with a slope of 10 °C min<sup>-1</sup> in an inert nitrogen atmosphere.

## 2.3. Lithium polysulphides adsorption test

To assess MXenes affinity towards lithium polysulphides species, responsible for the *shuttle effect*, an adsorption test with a polysulphide solution, followed by UV–Visible analysis of the supernatant solution, was performed. More in detail, 30 mg of each Ti<sub>3</sub>C<sub>2</sub> sample and of Ketjen Black (KJB; Nouryon, Ketjenblack EC-300 J) were put in contact with 4 mL of Li<sub>2</sub>S<sub>6</sub> 2 mM in 1,3-dioxolane (DOL; Sigma-Aldrich, anhydrous, 99.8%) and 1,2-dimethoxyethane (DME; Sigma-Aldrich, anhydrous, 99.5%) 1:1 v/v mixture. This solution was obtained by diluting a solution 0.25 M, prepared by mixing 0.5744 g of sulphur and 0.1149 g of lithium sulphide (Sigma-Aldrich, *battery grade*, 99.98%) in 10 mL of DOL/DME 1:1 v/v mixture, heating and stirring for 24 h at 70 °C in glovebox [73]

After 24 h, supernatant solutions put in contact with each sample were collected, diluted 1:5 and subjected to UV–Visible analysis to evaluate absorbance reduction due to adsorption of LiPS on MXenes. The same procedure has been done with the pristine 2 mM polysulphides solution, for direct comparison.

The UV–Vis absorption spectra were collected using a double-ray UV–Vis spectrophotometer (Jasco V-770 Spectrophotometer) within the spectral range of 200 - 900 nm and using pure DOL/DME 1:1 mixture as reference.

## 2.4. Electrochemical measurements

Working electrodes were prepared by solvent tape casting method. For electrochemical characterization of Ti<sub>3</sub>C<sub>2</sub>, slurries containing the four different samples, KJB and polyvinylidene fluoride (PVDF; Arkema, Kynar HSV 900) at a 8:1:1 as weight ratio and N-methyl-2-pyrrolidone (NMP; Honeywell, reagent grade, 99%) as solvent were prepared. In particular, 160 mg of MXene powder were firstly mixed with 20 mg of KJB in agate mortar and then transferred to an Eppendorf® tube containing 250 mg of a PVDF in NMP (solution 8% in weight), and 500  $\mu\text{L}$  of NMP. Then, the Eppendorf® tube was sealed and mixed in ball miller for 20 min at 15 Hz. In addition, a slurry made of only KJB and PVDF (at 9:1) ratio was prepared and used as reference.

Slurries were cast onto gas diffusion layer (GDL; sgl carbon, SIGRACET 39BB) through a film applicator (TQC Sheen) equipped with an adjustable doctor blade with a wet thickness of 200  $\mu\text{m}$  for symmetrical cyclic voltammetry and 100  $\mu\text{m}$  for Tafel plot tests, respectively. The same procedure was repeated to cast MXene slurries on aluminium carbon-coated foil (MTI Corp., aluminium: >99.9%, 15  $\mu\text{m} \pm 1 \mu\text{m}$ ; carbon-coating: 1  $\mu\text{m}$ , 0.5 g m<sup>-2</sup>) with 100  $\mu\text{m}$  wet thickness for chronoamperometry tests on lithium sulphide deposition. For full cell testing, slurries made of MXene or KJB/sulphur composites, KJB and PVDF (8:1:1 wt ratio) were cast on aluminium carbon-coated foil with 200  $\mu\text{m}$  thickness.

After solvent evaporation for 1 hour in oven (Mettler UN55) at 50

°C, disks of 15 mm of diameter were punched out, vacuum dried at 40 °C (in a Büchi Glass-Oven B-585) for 4 h, then transferred in a glovebox for cell assembly.

The electrochemical characterisation was carried out in CR2032 coin cells, assembled in different configurations depending on the type of test as described below:

- For symmetrical cyclic voltammetry, coin cells were assembled using two identical electrodes made by casting MXene samples or KJB on GDL and polypropylene (PP) polymeric membrane (Celgard 2500, 25 µm thickness, Ø 19 mm) as separator. As electrolyte were used 60 µL of lithium bis(trifluoromethanesulfonyl)imide (LiTFSI; Solvionic, 99.9%, under argon) 1.0 M and lithium exasulphide  $\text{Li}_2\text{S}_6$  0.125 M in a mixture of 1,3-dioxolane (DOL) and 1,2-dimethoxyethane (DME) 1:1 (v/v).
- For Tafel plot tests, coin cells were assembled using MXenes or KJB cast on GDL as working electrode, lithium chips (MTI Corp., 99.9%, Ø 16 mm) as counter electrode and PP polymeric membrane as separator. The electrolyte (60 µL) was LiTFSI 1 M, lithium nitrate ( $\text{LiNO}_3$ ; Aldrich, 99.9%, trace metals basis) 0.25 M and  $\text{Li}_2\text{S}_6$  0.0125 M in DOL/DME 1:1 mixture.
- For chronoamperometric lithium sulphide deposition tests, cells were assembled with MXene samples cast on aluminium carbon-coated foil as working electrode, lithium chips as counter electrode and PP membrane as separator. 60 µL of LiTFSI 1 M,  $\text{LiNO}_3$  0.25 M and  $\text{Li}_2\text{S}_6$  0.025 M in DOL/DME 1:1 mixture were used as electrolyte.
- Coins for full cell galvanostatic cycling were assembled using metallic lithium as anode, MXenes or KJB/sulphur composites cast on aluminium carbon-coated foil as cathode and PP membrane as separator. The electrolyte was a solution of LiTFSI 1 M and  $\text{LiNO}_3$  0.25 M in DOL/DME 1:1 mixture, with an electrolyte-to-sulphur (E/S) ratio of 15 µL  $\text{mg}^{-1}$ .

Symmetrical cyclic voltammograms were recorded using a BioLogic VSP-3e potentiostat. The measurement program involved 1 hour of rest followed by a cyclic potential scan at rate of 1  $\text{mV s}^{-1}$  between -1 V and +1 V, referring to cell open circuit potential. The measure was repeated three times.

Tafel plots were derived from linear sweep voltammetry (LSV) tests performed with the potentiostat between -50 mV and +50 mV, referring to open circuit voltage, after 1 hour of cell rest with scan rate of 0.200  $\text{mV s}^{-1}$ .

Lithium sulphide deposition tests were carried out using an Arbin BT-2000 battery tester, first performing a full galvanostatic discharge-charge cycle with a current of 100 µA to identify the exact supersaturation potential ( $E_{\text{sup}}$ ) of the cell, then discharging galvanostatically the cell until the potential value  $E_{\text{sup}}+10$  mV and then performing a potentiostatic discharge at potential  $E_{\text{sup}}-90$  mV until the measured current asymptotically reaches 0.

The galvanostatic cycling performances of the sulphur-containing cathodes were evaluated with Arbin BT-2000 battery tester, at room temperature in the 1.8 – 2.6 V vs.  $\text{Li}^+/\text{Li}$  potential range, performing 5 cycles at C-rate C/10 and 500 cycles at C/5. Applied current values were calculated from the theoretical capacity of sulphur (1672  $\text{mAh g}^{-1}$ ).

Potentiostatic Electrochemical Impedance Spectroscopy (PEIS) was performed on MXene/sulphur composite containing cells 1 hour after the assembly at voltage of around 2.7 V with a sinus amplitude of 5 mV in 1 MHz – 50 MHz frequency range using a BioLogic VSP-3e potentiostat. Then, a full discharge and charge cycle was performed at 0.1C before repeating the PEIS measurement at cell equilibrium voltage of 2.3 V. The obtained experimental data were analysed and fitted with ZView software according to equivalent circuit models found in literature [74]

Intermittent Current Interruption (ICI) test was performed on Arbin BT-2000 battery tester on MXene/sulphur composite containing cells, which were first assembled, rested for 1 hour and subjected to one discharge and charge cycle at 0.1C. The ICI protocol consisted of

applying 0.1C current pulses interspersed with resting periods of 10 s. During the short current interruptions, the cell voltage was sampled every 10 milliseconds to properly track the voltage evolution before the application of a new current pulse. The protocol was performed both in discharge and charge cycles. The obtained data were analysed according to the method described in literature to track the evolution of the cell internal resistance and the coefficient of diffusion resistance [75,76]

### 3. Results and discussion

#### 3.1. Structural and morphological characterisation of $\text{Ti}_3\text{C}_2\text{T}_x$ MXenes

Four different MXene samples were synthesised as reported in Table 1 in the Experimental Section. X-ray diffraction (XRD) analysis was performed on all samples to confirm the formation of the MXene phase and to assess structural differences as a function of the different synthesis parameters.

Fig. 1a shows the diffractograms registered for each MXene sample compared with that of  $\text{Ti}_3\text{AlC}_2$  MAX phase, used as precursor. Dashed vertical lines highlight the main reflexes of MAX phase and their (hkl) planes, responsible for diffraction. The almost complete disappearance of reflexes related to planes (101), (103), (105) and, particularly, (104) in  $\text{Ti}_3\text{C}_2$  samples demonstrates a nearly total conversion from MAX to MXene phase. In contrast, plane (002), (004) and (110) reflexes, remain detectable in all samples, although shifted in  $2\theta$  values, lower for (002) and (004) and higher for (110), and broadened as a consequence of the material exfoliation. In particular, lower  $2\theta$  value for reflex (002) is due to the etching of aluminium atoms from the precursor and to the enhancement of *d*-spacing between planes and of lattice parameter *c*.

From the  $2\theta$  values of the (002) reflexes, the *d*-spacing for each sample was calculated using Bragg's equation, obtaining values of 9.43 Å for MX\_01, 9.70 Å for MX\_02, 9.56 Å for MX\_03, and 9.64 Å for MX\_04. The greater *d*-spacing values observed for the samples prepared with lower hydrofluoric acid concentrations (MX\_01 and MX\_03) highlighted the detrimental effect of higher acid concentration on interplane distances [77] As also shown in Fig. 1a, reflexes (004) and (008), relative to the characteristic multilayered structure of MXenes, have the same shift pattern as reflex (002) between the four different samples because of their dependence only on lattice parameter *c*, expanded after the synthesis [78]

All synthesised materials were morphologically characterised by FESEM, supported by EDX analysis (reported in Table S1) which roughly confirmed the expected atomic compositions of the synthesised samples.

Fig. 1b compares FESEM micrographs of each sample with magnification 1k and 25k. At lower magnification (e.g. 1k), as visible in the micrographs in Fig. 1b (left), each sample is composed of micrometric particles with variable sizes. However, carefully observing the particle size dispersion, it can be noted that for sample MX\_03, and partially for MX\_01, several smaller particles are present, showing higher polydispersity inside the sample, probably due to the lower synthesis temperature [77]

From micrographs at higher magnification (25k), it is possible to see the characteristic “accordion-like” structure of MXenes for all the samples. However, higher acid concentration leads to more damaged structures and less regular space between material planes.

The particle size distribution results for each MXene sample are summarised in Table 2 as mean value, standard deviation, D10, D50 and D90 for four different parameters: major and minor particle axis, Feret diameter and aspect ratio. As observed in the micrographs in Fig. 1b, samples MX\_01 and MX\_03 are characterised by smaller particles, as indicated by the lower mean values for both particle axes and Feret diameter when compared with the other two samples. These samples also exhibit slightly lower aspect ratio values, suggesting the presence of less elongated particles. In addition, from the particle size distribution statistics, it is clear that the main difference between the samples obtained with lower and higher acid concentration is due to the coarser

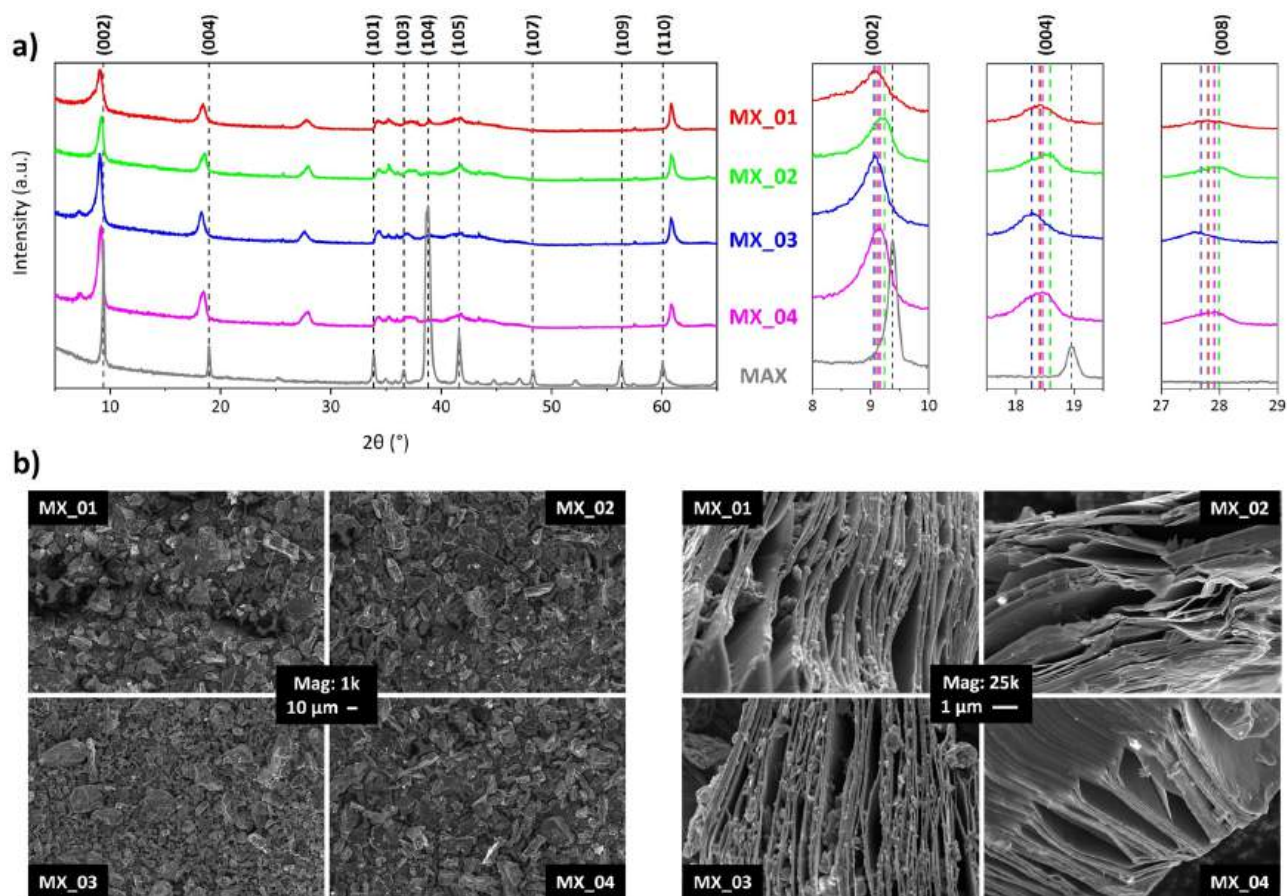


**Fig. 1.** a) Comparison between diffractograms obtained from MAX phase and MXene samples and zoom of (002), (004) and (008) reflexes together with shift pattern among the four different samples; b) MXene samples micrographs at 1k and 25k magnification.

**Table 2**

Particle size distribution statistics derived from FESEM micrographs for each MXene sample.

Sample	Parameter	Mean	St. Dev.	D10	D50	D90
MX_01	Major Axis ( $\mu\text{m}$ )	9.6	6.8	2.1	8.6	18.5
	Minor Axis ( $\mu\text{m}$ )	5.9	4.0	1.1	5.7	11.0
	Feret Diameter ( $\mu\text{m}$ )	10.1	6.6	2.2	9.1	18.4
	Aspect Ratio	1.75	0.76	1.18	1.55	2.46
MX_02	Major Axis ( $\mu\text{m}$ )	10.6	9.0	1.8	8.8	21.6
	Minor Axis ( $\mu\text{m}$ )	6.2	5.3	0.9	5.4	13.3
	Feret Diameter ( $\mu\text{m}$ )	11.3	9.2	1.9	9.6	23.3
	Aspect Ratio	1.89	0.96	1.22	1.64	2.83
MX_03	Major Axis ( $\mu\text{m}$ )	8.1	6.4	1.4	7.4	16.4
	Minor Axis ( $\mu\text{m}$ )	5.1	3.9	0.9	5.0	10.2
	Feret Diameter ( $\mu\text{m}$ )	8.6	6.7	1.5	8.1	17.3
	Aspect Ratio	1.72	0.73	1.17	1.52	2.39
MX_04	Major Axis ( $\mu\text{m}$ )	10.8	7.0	2.3	10.2	19.7
	Minor Axis ( $\mu\text{m}$ )	6.6	4.4	1.1	6.3	12.2
	Feret Diameter ( $\mu\text{m}$ )	11.6	7.4	2.5	11.1	21.2
	Aspect Ratio	1.84	0.88	1.20	1.62	2.63

fraction of particles since the D90 value related to Feret diameter is lower than  $20 \mu\text{m}$  for samples MX\_01 and MX\_03, while higher than  $20 \mu\text{m}$  for samples MX\_02 and MX\_04.

XPS analysis was performed to evaluate the surface composition of the MXene materials. In the survey spectra (Figure S1a), the F 1 s peak, absent in the MAX phase, emerges in all MXene samples, consistently with fluorine termination following HF etching [21,79,80]. The Al 2p and Al 2s signals observed in the MAX precursor cannot be detected in MXene samples due to their almost complete removal upon etching treatment. Additional expected signals associated with MXenes, such as C 1s,

O 1s, Ti 3p, and Auger features (F KLL, O KLL, Ti LMM, C KLL), are clearly observed in wide spectra.

High-resolution Ti 2p spectra provide detailed insight into the Ti chemical environment. Ti 2p spectra of MXene samples (Fig. 2a, b, c and d) are similar and markedly differ from that of the MAX phase, reported in Figure S1b. Whereas Ti 2p spectrum in MAX phase is characterised by a carbide Ti-C contribution and oxide features, the MXenes spectra require multiple components associated with different surface terminations. For example, for MX\_01, the Ti 2p<sub>3/2</sub> components at 455.1, 456.0, 457.0, and 458.0 eV are assigned, respectively, to C-Ti-(O,O,O), C-Ti-(O,O,F), C-Ti-(O,F,F), and C-Ti-(F,F,F) environments, while the higher-binding-energy contribution at  $\sim 459.6$  eV is attributed to titanium oxyfluoride species, TiO<sub>2-x</sub>F<sub>x</sub>. These terminations, as observed in a previous study [81], are beneficial for the catalysis of sulphur redox reactions because of high fluorine electronegativity, which tunes the positive charge of exposed Ti metal sites, enhances interaction with sulphurised species and traps electrons generated during Li<sub>2</sub>S oxidation. Similar component distributions are observed for MX\_02, MX\_03, and MX\_04, as summarised in Table S2 (only Ti 2p<sub>3/2</sub> data are listed). These energy assignments agree well with prior XPS studies of Ti<sub>3</sub>C<sub>2</sub>T<sub>x</sub> [82]. This multi-component fitting strategy for the Ti 2p region has been reported and recommended in the literature for MXene systems [83]. Here, the experimental spectra display several characteristic features that can be discussed within this fitting framework. Anyhow, it should be noted that, as evidenced in recent literature about the XPS analysis of Ti<sub>3</sub>C<sub>2</sub>T<sub>x</sub> [69], the identified Ti 2p components represent “effective” Ti environments with mixed coordination and do not correspond to “pure” -O, -OH, or -F terminations on individual Ti sites. Thus, they do not allow a quantitative determination of -O/-F termination ratios, but provide a

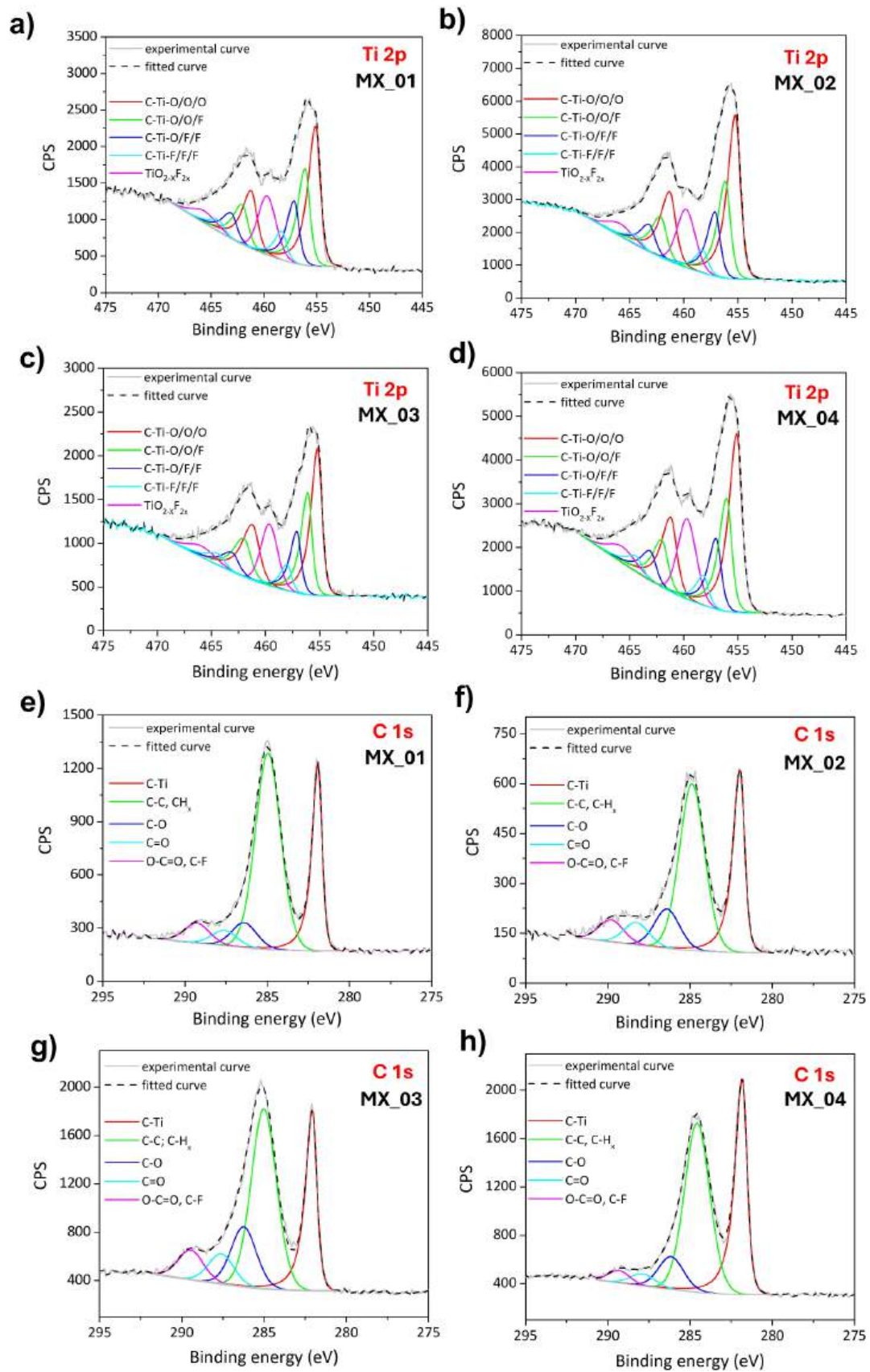


**Fig. 2.** MXene characterisation by XPS. High-resolution Ti 2p spectra recorded for a) MX\_01; b) MX\_02; c) MX\_03 and d) MX\_04 samples. High-resolution C 1 s spectra recorded for e) MX\_01; f) MX\_02; g) MX\_03 and h) MX\_04 samples.

qualitative trend of the relative abundance of oxidized vs fluorinated Ti species.

First, for a given Ti oxidation state, the binding energy difference between Ti–O and Ti–F coordination is reported to be approximately constant ( $\sim 2.9$  eV) [83]. In all MXenes studied here, the energy separation between the C–Ti–(O,O,O) and C–Ti–(F,F,F) components lies within 2.9–3.0 eV, lending confidence to the component assignments. The spin–orbit splitting ( $\Delta Ti\ 2p$ ) was around 6.1 eV for  $Ti_3C_2T_x$ -related components and 5.6 eV for oxide and oxyfluoride species, as expected for these materials. Second, the presence of fluorine terminations is independently confirmed by the F 1s spectra. As shown for the MX\_01 sample in Figure S2 (Supporting Information), a dominant peak at  $\sim 684.9$  eV is observed and assigned to C–Ti–F<sub>x</sub> species, in agreement with previous reports on Ti-based MXenes [82]. In addition to this main component, a weaker high-binding-energy feature at approximately 686–687 eV is detected and attributed to AlF<sub>x</sub> or Al(OH)<sub>x</sub> species, which are commonly reported as etching byproducts in HF-etched  $Ti_3C_2$  materials. Similar F 1s spectral features are observed for all MXene samples analysed in this study.

Additional insight into the obtained materials can be gained from the analysis of the high-resolution C 1s spectra (Fig. 2e, f, g and h). In particular, comparison with the spectra recorded for the corresponding MAX phase, shown in Figure S1c (Supporting Information), clearly reveals a substantial modification of the spectral profile after the etching treatment. While the MAX phase is characterised by a dominant

contribution associated with adventitious carbon, the MXene samples exhibit a much more evident and prominent C–Ti component. This change reflects the selective removal of the Al-layer and the consequent exposure of the Ti–C bonds within the MXene structure, consistently reported as a key spectroscopic fingerprint of successful MAX-to-MXene conversion [84].

As an example, the high-resolution XPS spectrum in the C 1s region of the MX\_03 powder (Fig. 2g) can be fitted by five components located at approximately 282.0, 285, 286.4, 287.8, and 289.4 eV. These features are attributed to C–Ti, C–C, C–O, C=O, and O–C=O (or, in part, C–F as this component lays over a wide energy range) species, respectively, in good agreement with previous reports on Ti-based MXenes obtained by HF etching or related routes [83]. A similar C 1s spectral fitting is observed for all MXene samples investigated in this work (Fig. 2b–d), indicating a consistent surface chemistry across the series.

The presence of oxygen-containing carbon species is commonly observed in MXenes and can be attributed to partial surface oxidation during synthesis and handling, resulting in the formation of TiO<sub>x</sub> species, as well as to unavoidable adventitious carbon contamination upon air exposure [85]. Notably, the C–Ti component at  $\sim 282.0$  eV remains clearly resolved in all samples and constitutes one of the most reliable spectroscopic fingerprints of the MXene carbide backbone. The assignment of this feature to C–Ti bonds is particularly robust, as its binding energy is largely insensitive to the nature of the surface terminations bonded to Ti (–O, –OH, –F) and is instead primarily governed by the

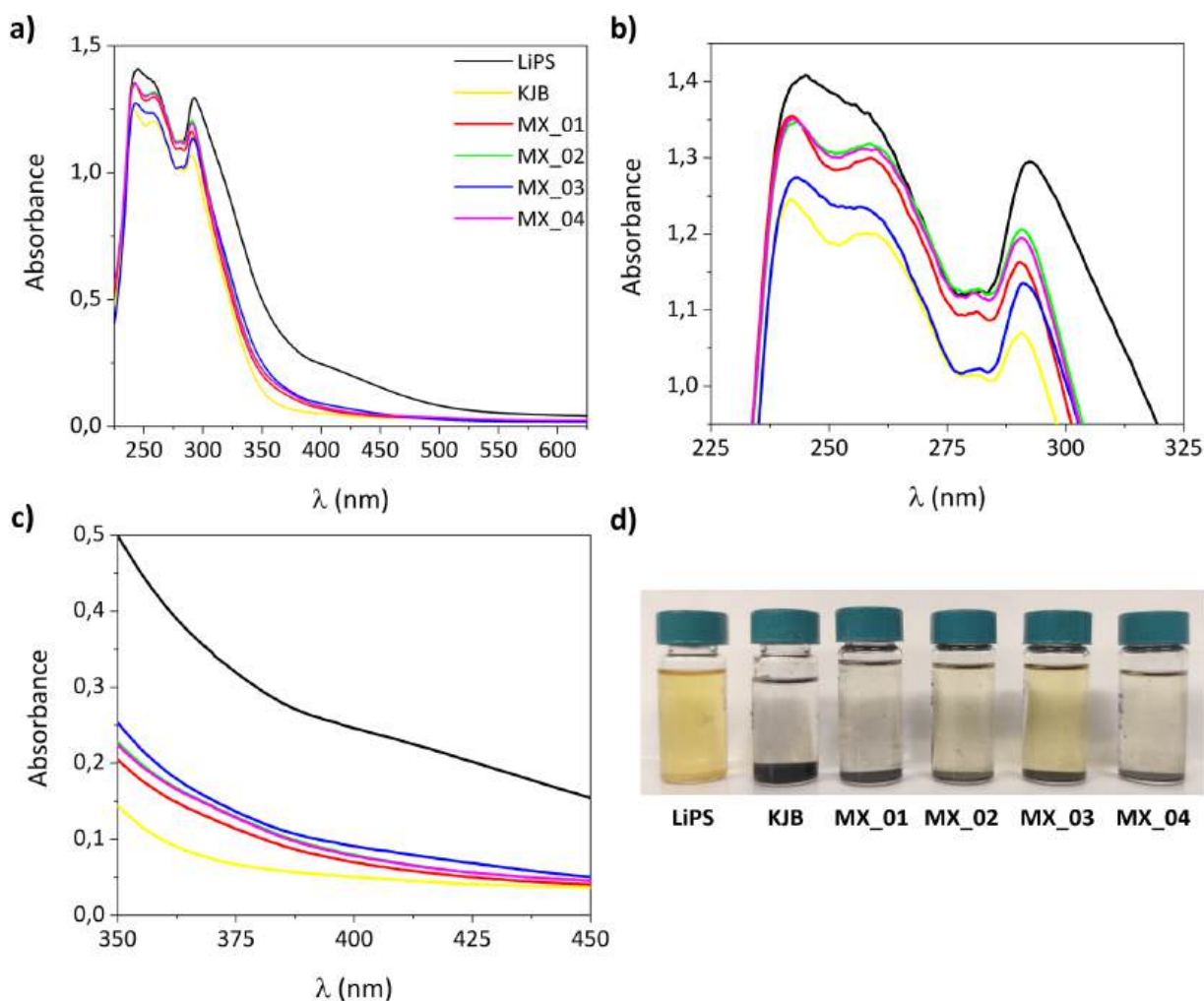


**Fig. 3.** a) UV–Vis spectra recorded in 225–625 nm range of 0,4 mM polysulphides solution before (LiPS) and after contact with KJB and MXene samples for 24 h; b) UV region zoom between 225 and 325 nm of spectra presented in Figure 3a; c) UV and visible region zoom between 350 and 450 nm of spectra presented in Figure 3a; d) Photography of vials containing LiPS solution before and after contact with each sample for 24 h.

underlying carbide framework. This behavior has been consistently documented in detailed XPS studies of  $Ti_3C_2T_x$  and related MXenes, further supporting the validity of the present assignments [83]. Among the fitted components, the C–C peak at  $\sim 284.9$  eV is also intense, while the oxygen-containing functionalities constitute minor components.

### 3.2. Lithium polysulphides adsorption test (UV–Vis)

Considering the different morphology of the four samples and their surface composition and, in order to evaluate the possible and different interaction of MXenes with lithium polysulphides, adsorption tests followed by UV–Vis spectrophotometric analysis were carried out. Fig. 3a shows UV–Vis absorbance spectra of lithium polysulphides solutions put in contact 24 h with  $Ti_3C_2$  samples and KJB and of the original solution. All solutions present a clear reduction of absorbance after the adsorption test, as can also be seen in Fig. 3d, revealing good affinity of the materials towards polysulphide species. In each spectrum, three main absorption bands are observed: one between 250 and 280 nm, attributed to elemental sulphur ( $S_8$ ); one between 290 and 300 nm, ascribed to polysulphide  $S_6^{2-}$  (highlighted in Fig. 3b); and one in the visible region between 400 and 440 nm, corresponding to short-chain polysulphide  $S_4^{2-}$  (Fig. 3c), which is responsible for the colour of the solution [86].

Carefully analysing the UV spectra, KJB shows the greatest adsorption capacity among the considered materials due to its high porosity, but since it can perform only physisorption phenomena like all carbonaceous materials, the interactions with lithium polysulphides result

weaker [87]. On the contrary, MXenes, thanks to their superficial functional groups and Lewis acidity of unsaturated titanium atoms, show a stronger chemisorption phenomenon with lithium polysulphides. More specifically, MX\_03 exhibits the highest absorbance decrease in the UV region, indicating a stronger affinity for elemental sulphur and long-chain polysulphide,  $S_6^{2-}$ . However, the solution remains yellowish, suggesting a lower affinity for short-chain polysulphide,  $S_4^{2-}$ . On the contrary, MX\_01 showed a better affinity for short-chain polysulphide, as demonstrated by the greatest bleaching of solution colour. For samples MX\_02 and MX\_04, absorption spectra show similar behaviour towards polysulphide species and the lower affinity with long-chain ones.

### 3.3. Electrochemical characterisation of $Ti_3C_2T_x$ samples

In order to evaluate, in addition to the chemo-physical interaction of the different MXenes with the polysulfides, also their possible catalytic activity, cyclic voltammetry analyses in a symmetric cell were carried out.

Fig. 4a compares cyclic voltammogram results obtained for symmetrical cells of each MXene sample. Each voltammogram shows two oxidation (anodic branch) and two reduction (cathodic branch) peaks with some slight differences for peak current intensities and position. Particularly, samples MX\_03 and MX\_04 show the highest values of peak current and the lowest potential shifts in relation to open circuit voltage, nominally equal to 0, implying that a lower overpotential is required to start the electrochemical reactions. MX\_01 and MX\_03, which were

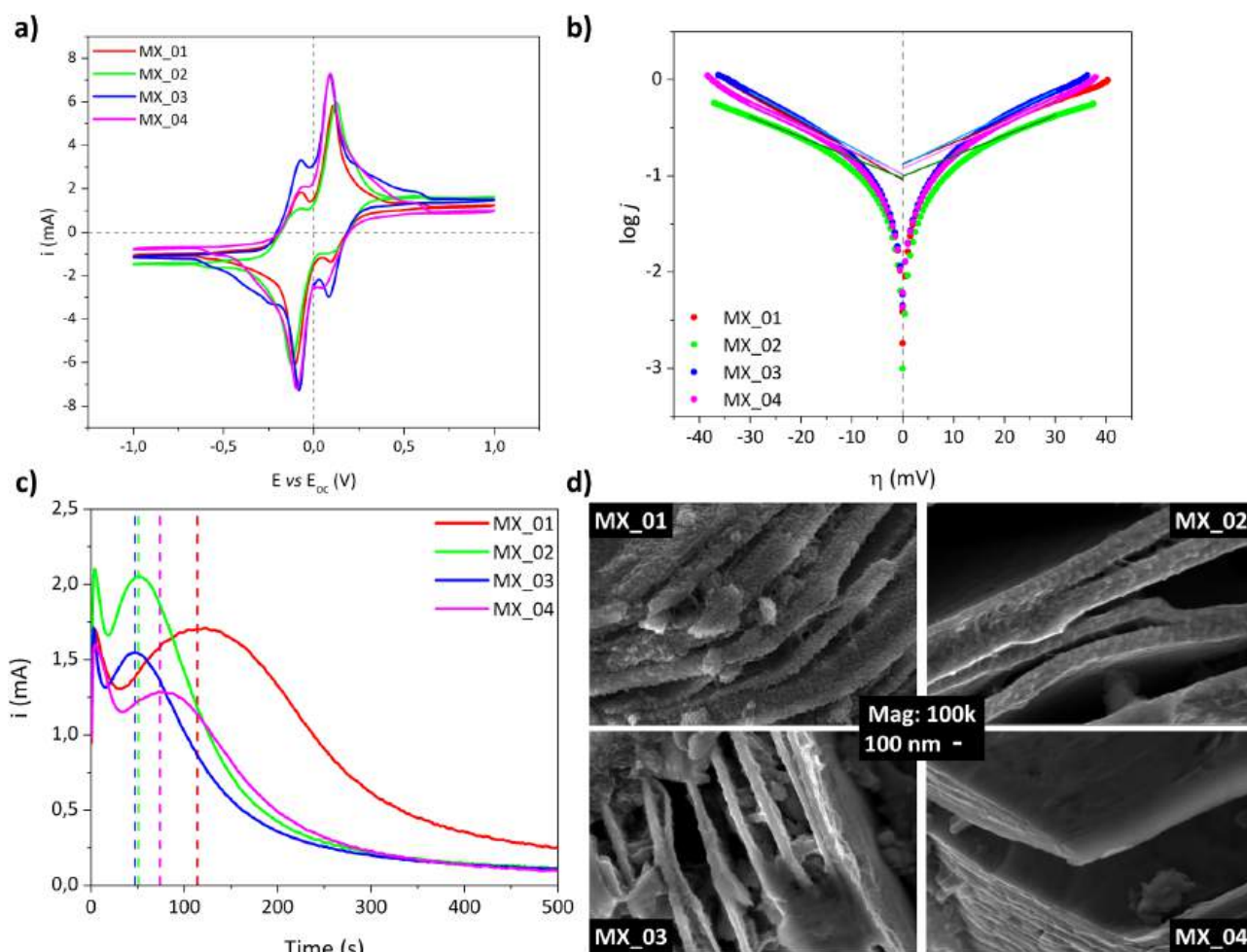


**Fig. 4.** a) Symmetric cyclic voltammograms obtained for each MXene sample; b) Tafel plots derived from LSV measurements for each MXene sample; c) Lithium sulphide deposition chronoamperometric curves and relative peak time obtained for each MXene sample; d) Micrographs of electrodes containing each  $Ti_3C_2$  sample after lithium sulphide deposition tests with 100k magnification.

obtained with lower HF concentration, are characterised by a more defined first peak in both CV branches. Table 3 reports potential values for the observed peaks in each cyclic voltammogram, which were calculated by evaluating the reversal of first derivative curves. The comparison of the peak potentials together with the whole CV profile can be compared to the literature to identify the polysulphides conversion reaction occurring in the cell [88,89]

In particular, the first peak ( $E_{O1}$  and  $E_{R1}$ ) with lower intensity in both cathodic and anodic branch can be attributed to the conversion between  $Li_2S_8$  and  $Li_2S_6$  species, while the second and most intense peak ( $E_{O2}$  and  $E_{R2}$ ) is due to the conversion between  $Li_2S_6$  and  $Li_2S_4$ . In addition, a broad shoulder at higher overpotentials can be seen, especially for MX\_03, indicating the process of solid  $Li_2S$  formation from short-chain lithium polysulphides. This can be easily linked with the kinetics of  $Li_2S$  deposition process which will be discussed later.

Fig. 4b shows the Tafel plots derived from LSV measurements for each sample together with interpolation lines obtained from both cathodic and anodic branch considering, respectively, overpotential intervals of  $-20 \div -30$  mV and  $20 \div 30$  mV. In general, the exchange current density values fall within the range  $0,0910 \div 0,134$  mA cm<sup>-2</sup> for all samples; however, some significant differences can be observed. More in detail, MX\_01 exhibits the highest anodic exchange current density, but a lower value for the cathodic processes, resulting in an evident asymmetry between the two branches. On the contrary, MX\_02, presents good symmetry, but low  $j_0$  values overall, while MX\_03 and MX\_04 show similar results, showing good symmetry for the profile and higher exchange current density values. In particular, MX\_03 is characterised by a higher exchange current density for the oxidation process. All materials have a higher value for the exchange current in the anodic branch of the plot, which can suggest a better catalytic activity for the oxidation of polysulphide species.

Fig. 4c compares chronoamperometric curves for lithium sulphide deposition of the four  $Ti_3C_2$  samples, considering electrodes with comparable mass loading, while

Table 4 reports values of deposition specific capacity (SC) and of time needed to reach peak current ( $t_m$ ). Sample MX\_01 shows the highest value of specific capacity for  $Li_2S$  deposition, but also the highest  $t_m$ , which means worst process kinetics among the synthesised materials. These results are consistent with those obtained in the polysulphides adsorption test previously presented, where MX\_01 demonstrated a better affinity towards short-chain species, whose reduction is responsible for the deposition process. The strong interaction between MX\_01 and  $S_4^{2-}$  probably leads to its accumulation on MXene surface, retarding its reduction, but enabling the formation of a higher amount of precipitate. For the same reason, sample MX\_03 has the fastest deposition kinetics (lowest value of  $t_m$ ) because of its low affinity towards short-chain polysulphides, which are quickly reduced, forming lithium sulphide. MX\_02, however, presents an intermediate behaviour in terms of deposition-specific capacity and kinetics overall. MX\_04, instead, is characterised by the lower specific capacity, although not too different from MX\_03, but with a higher  $t_m$  value and a curve shape more similar to MX\_01.

Experimental results obtained from deposition tests have then been compared to four theoretical deposition models, which explain the morphology of the final solid product on the substrate surface. The considered models are Bewick-Fleischman-Thirsk model [90], which

**Table 3**  
Potential values for anodic and cathodic peaks for symmetrical cyclic voltammograms shown in Fig. 4a.

Sample	$E_{O1}$ (V)	$E_{O2}$ (V)	$E_{R1}$ (V)	$E_{R2}$ (V)
MX_01	-0,0694	0108	0,0939	-0103
MX_02	-0,0694	0125	0,0613	-0124
MX_03	-0,0705	0,0896	0,0837	-0,0824
MX_04	-0,0544	0,0917	0,0425	-0,0943

**Table 4**

Specific capacity and peak time values derived from chronoamperometric deposition curves presented in Fig. 4c.

Sample	SC (mAh g <sup>-1</sup> )	$t_m$ (s)
MX_01	321,91	114
MX_02	242,81	51
MX_03	201,48	47
MX_04	192,94	73

accounts for both instantaneous (2DI) and progressive (2DP) bidimensional deposition and Scharifker-Hills model [91], that explains instantaneous (3DI) and progressive (3DP) tridimensional deposition. Figure S3 shows the comparison between experimental data and the four models for each MXene sample, while the corresponding equations are reported in Table S3. For all  $Ti_3C_2$  samples the experimental deposition curve matches with 3DI model, in which nucleation and proliferation processes are consecutive and lead to the formation of several and identical lithium sulphide “islands”, but only for normalised time values,  $t/t_m$ , lower than 3. For higher values, experimental current densities normalised by peak current density,  $j/j_m$ , significantly drops and shows an intermediate trend between 2D and 3D models. This behaviour is probably attributed to lithium sulphide islands coalescence, with the subsequent formation of a pseudo-bidimensional film which passivates MXene surface and inhibits any further growth of the precipitate. In general, experimental deposition data show a hybrid 2D-3D behaviour if compared to the considered models, probably due to the combination of substrate polarity and the presence of DME as co-solvent, which induce the formation of bidimensional precipitates, and the use of electrolyte salts as LiTFSI and  $LiNO_3$ , that favours a 3D growth thank to their high Donor Number (DN) [92]

Furthermore, cells for each MXene sample were disassembled in glovebox after deposition tests and the recovered cathodes were analysed through FESEM to experimentally assess lithium sulphide deposition morphology. Fig. 4d shows micrographs of different cathodes, acquired at 100k. From the micrographs, it is evident, especially for MX\_01 and MX\_02 because of their higher deposition specific capacity, the presence of small spherical particles that cover almost all the surface of MXene sheets, coherently with the hypothesis made from models analysis, although the morphology seems more 3D rather than 2D. For samples MX\_03 and MX\_04, instead, the surface is smoother, but a certain coverage by  $Li_2S$  nanoparticles is still visible. This can confirm the significant influence of  $Ti_3C_2$  MXenes, due to their abundant polar sites, as effective substrates for lithium sulphide deposition.

The more 3D morphology observed is in contrast with the typical 2D morphology favoured by the used electrolyte, as previously stated and reported in other experimental studies [93–95]. However, the coexistence of electron-rich environments and fluorine-modulated sites in MXenes can favour 2D–3D hybrid deposition behaviour. Specifically, the fluorinated Ti sites can promote polysulphide adsorption and  $Li_2S$  nucleation through enhanced Lewis acidity, while the preserved MXene conductive framework guarantees the electron transport during subsequent  $Li_2S$  growth. Consequently, a hybrid 2D–3D deposition process can alleviate premature surface passivation while maintaining efficient  $Li_2S$  deposition kinetics [92,96–99]

These analyses highlight the relevance of the heterogeneous nature of the MXene surface chemistry. In fact, a controlled amount of oxidised and fluorinated species can promote stronger adsorption of lithium polysulphides while still preserving acceptable electronic conductivity [64,81,100]. Specifically, increased surface oxygenation enhances surface polarity, thereby favouring the interaction with polysulphides. At the same time, the relatively lower fraction of fluorinated species helps to maintain a sufficiently conductive surface.

In addition to surface functionalisation, the morphology of the samples must also be considered. More exfoliated structures with smaller particles provide a larger accessible surface area for interaction

with sulphur and lithium polysulphides. Therefore, the electrochemical behaviour cannot be attributed solely to surface chemistry; rather, it arises from the combined effect of morphology and surface composition, both of which are strongly influenced by the etching conditions.

Different surface terminations of MXenes are also known to affect the  $\text{Li}_2\text{S}$  deposition mechanism. In general, a higher degree of oxidation combined with a more irregular and defective morphology may increase the density of active sites available for polysulphide adsorption, while the specific surface chemistry simultaneously influences the nucleation and growth of  $\text{Li}_2\text{S}$  [64,100]

### 3.4. Structural and morphological characterisation of MXene/sulphur composites

After characterising the different MXenes and evaluating their properties as potential catalytic agents for polysulphides conversion and  $\text{Li}_2\text{S}$  deposition, the materials were employed as sulphur hosts in the cathode manufacturing process, achieved by finely mixing them with sulphur in a ball miller (1 h, 10 Hz; sulphur/MXene ratio of 3:1 wt.%) and then performing the melt diffusion process in muffle furnace at 155 °C for 5 h in an inert argon atmosphere.

Thermogravimetric analysis (TGA) was performed on MXene/sulphur composites after the melt diffusion process to verify the effective content of sulphur in cathodic materials, as reported in Figure S4a–d. For all samples the sulphur content is close to the nominal value and

amounts to 74,9% for MX\_01, 75,2% for MX\_02, 75,3% for MX\_03 and 74,5% for MX\_04. Table S4, reports the temperature interval in which sulphur loss occurs for each sample and temperature value corresponding to the first derivative minimum and so the highest rate of sulphur loss.

Structural and morphological analysis of sulphur-containing cathodic materials, were performed through XRD and FESEM. From diffraction patterns reported in Figure S5, it is possible to appreciate both sulphur and MXenes reflexes. *d*-spacing values for all the composites were calculated as for the bare MXene phases, showing that the infiltration of sulphur between the planes of the material results in a more homogeneous spacing (9.65 ÷ 9.70 Å for the different samples). In addition, sulphur reflexes are systematically shifted towards lower 2θ values because of the crystalline lattice expansion due to the melt diffusion process and the interaction with the MXene phase. This interaction is clearly visible in FESEM micrographs at 10k and 25k magnification shown in Figure S6 and Figure S7, respectively, where the sulphur matrix not only incorporates MXene particles, but also penetrates into their characteristic “accordion-like” structure.

To investigate the nature of this interaction, MXene/sulphur composites were also investigated by XPS. Survey spectra in Figure S8a (Supporting Information) clearly reveal the presence of sulphur through the appearance of S 2p and S 2s signals, absent in pristine MXenes. High-resolution Ti 2p spectra (Fig. 5), in addition to the Ti–C–(O,F) components discussed before, reveal additional features possibly suggesting

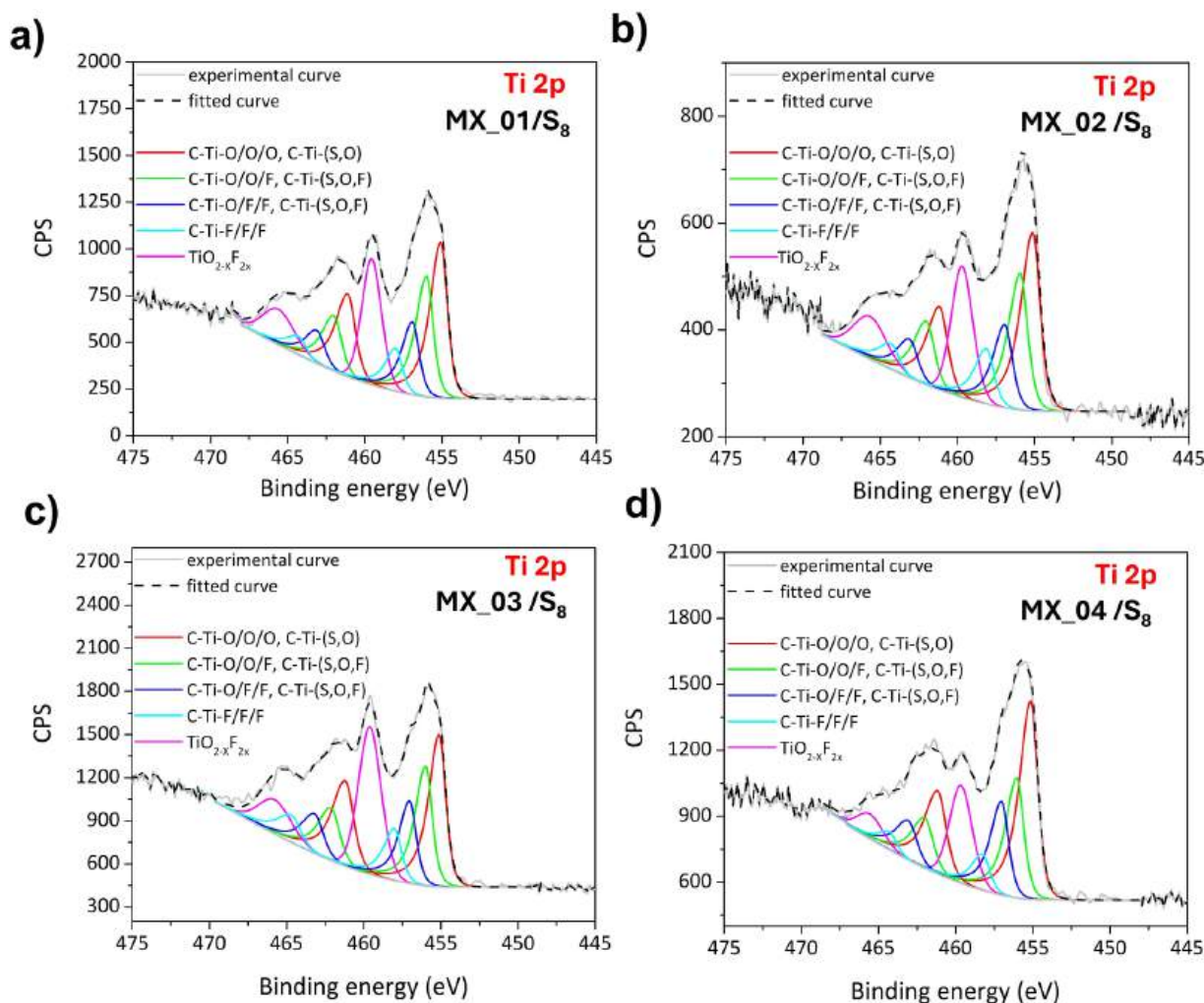


Fig. 5. MXene/sulphur composite characterisation by XPS. High-resolution Ti 2p spectra recorded for a) MX\_01/S<sub>8</sub>; b) MX\_02/S<sub>8</sub>; c) MX\_03/S<sub>8</sub> and d) MX\_04/S<sub>8</sub> samples.

the formation of hybrid C–Ti–(O,S) environments. Under the synthesis conditions employed, it is plausible that a fraction of the oxygen atoms in the MXene surface terminations are partially replaced by sulphur species, leading to the formation of Ti–S bonds at the surface. Although Ti–S–related spectral features cannot be unambiguously distinguished from the existing Ti–O/F components in the Ti 2p region, due to their strong overlap, their presence is supported by the analysis of the high-resolution S 2p spectra. The S 2p fitting in Figure S8b reveals, in addition to the contribution associated with elemental sulphur (S<sub>0</sub>), an additional S 2p doublet attributed to sulphur bonded to titanium. The S 2p<sub>3/2</sub> component is centred at approximately 162.7 eV. This binding energy lies within the range commonly reported for Ti–S bonding in titanium sulphides and surface Ti–S species ( $\approx 162.5 \pm 0.2$  eV) [23]. The observation of this feature indicates the formation of Ti–S bonds at the MXene surface, consistent with partial substitution of Ti–O terminations by sulphur species, as previously reported for sulphur-functionalised MXenes and related Ti-based systems [23]. The presence of Ti–S bonding is particularly relevant for stabilizing sulphur within the composite material by providing chemical anchoring sites. In contrast, the higher-binding-energy S 2p component observed around  $\sim 168$  eV is attributed to oxidised sulphur species or polysulphide-related environments, likely arising from interactions between sulphur species and the surface during the sulphur loading process [101].

### 3.5. Electrochemical characterisation of Ti<sub>3</sub>C<sub>2</sub>T<sub>x</sub> samples

Fig. 6a and Fig. 6b show the results of electrochemical characterization of MXene/sulphur composites obtained for each Ti<sub>3</sub>C<sub>2</sub> sample through galvanostatic cycling tests, consisting of 5 cycles at C/10 and 100 cycles at C/5. To better elucidate the role of different MXene within the cathode formulation, the specific capacity and C.E. values were averaged over four independent replicates and reported with 95% confidence intervals, calculated based on a Student's *t*-distribution.

As observed, the C.E. shows an unexpectedly high value, around 120%, during the first cycle, meaning a partially irreversible discharge capacity. However, from the second cycle onward, the CE stabilises around 99% for all samples, indicating good reversibility of the sulphur redox processes. Analysing the first cycle discharge curves reported in Fig. 7a (black dotted lines) for each MXene sample, it is clear that the irreversible specific capacity delivered is always linked to the first discharge plateau, which is correlated to sulphur solubilization from the cathode structure and its reduction to soluble polysulphide species. In addition, these CE values >100% indicate that, during the first cycle discharge, a certain amount of lithium ions diffuse into the cathode but they are not released during the charge process. This phenomenon was previously observed in lithium-sulphur cells characterised by lean electrolyte conditions (E/S of 5  $\mu\text{L mg}^{-1}$ ), where the lack of electrolyte results in a high concentration of polysulphide species and high viscosity of the solution, consequently reducing electrolyte conductivity and lithium ions diffusivity [102]. In our case, the electrolyte-to-sulphur ratio adopted was 15  $\mu\text{L mg}^{-1}$ , so this high value of CE is reasonably ascribable to the employment of Ti<sub>3</sub>C<sub>2</sub> MXenes as sulphur host, which tend to confine into the cathodic structure polysulphide species, produced during the first discharge, thanks to the good affinity with them. On one side, this behaviour helps to mitigate the shuttle effect, enhancing cell stability, on the other hand, it leads to electrolyte saturation with lithium polysulfides, which reduces overall ionic conductivity, limiting complete sulphur utilisation and effectively causing the system to operate under conditions similar to those observed in lean-electrolyte cells.

Specific capacity values were particularly differ during initial cycles (around 25 for MX\_02 and 50 for MX\_04) of the galvanostatic cycling, while for the remaining cycles they were more stable and quite similar for all MXenes, except for sample MX\_01. More in detail, during the first five cycles at C/10, adopted here as formation cycles, sample MX\_03 delivers higher performance in terms of specific capacity (around 600

mAh g<sup>-1</sup>), followed by MX\_02 and then by MX\_01 and MX\_04. Increasing the C-rate to C/5, all MXene-based cathodes, except the one containing MX\_03, exhibited a rising trend in specific capacity over cycling. This behaviour is probably due to the progressive activation and redistribution of active sulphur, resulting from the repeated dissolution and redeposition of the active material. Such capacity growing trend ended after approximately 25 cycles for MX\_02 and around 50 cycles for MX\_04, while MX\_01 showed a continuous growth throughout the entire testing period. Another possible hypothesis is that the growth in specific capacity during cycling is linked to a dynamic change of cathode gravimetric density and porosity during the process induced by electrolyte uptake and electrode swelling due to sulphur volume change during lithiation and delithiation, as previously observed in lean electrolyte systems with DOL/DME solvents, which easily solubilise polysulphide species [103]. This is consistent with the previous assumption about the high observed initial C.E., which suggests a behaviour similar to lean electrolyte systems for MXenes.

Another interesting difference among the four samples is the confidence interval associated with specific capacity values: the cathode containing MX\_01 show high variability, especially during the formation cycles and after 70 cycles probably due to inhomogeneous and non-optimal sulphur distribution within the cathode. In contrast, the composites containing MX\_02 and MX\_04 show high variability during the “activation cycles”, but the error bars significantly narrow once stable specific capacity values are reached, typically after 40–50 cycles. As an example, for sample MX\_03 the confidence interval is almost constant, showing just a small narrowing trend over the cycles. The differences in terms of performance observed among the four materials are probably influenced by the dispersion of MXene and sulphur after thermal treatment, as shown in the FESEM micrographs reported in Figure S6 and Figure S7 discussed previously. In fact, samples with accessible and homogeneously distributed Ti<sub>3</sub>C<sub>2</sub>T<sub>x</sub> particles exhibit better electrochemical performance compared to those in which the lamellar MXene structures seem embedded within sulphur aggregates. The different distribution and consequent interaction between MXene and sulphur implies a different activation period to enable structural reorganization of the active material.

However, a direct comparison of the average specific capacity values, as shown in Fig. 6b, reveals that sample MX\_03 exhibits a higher average capacity and a more linear and stable trend compared to the other samples. It can be seen that the capacity of MX\_03 remains above 400 mAh g<sup>-1</sup> for the entire cycling process. After approximately 25 cycles at C/5, sample MX\_02 exhibited progressive stabilization, reaching specific capacity values, after 100 cycles, only slightly lower than those of sample MX\_03. In contrast, samples MX\_01 and MX\_04 showed a slower activation process and lower capacity values, suggesting a different interaction behaviour with sulphur. This is also evident from the histogram shown in Fig. 6c, which compares mean specific charge capacity values with their confidence interval among the first, the fiftieth and the hundredth cycle at C/5 for the different MXene samples.

To better evaluate the behaviour of different MXenes in the charging and discharging process of Li-S cells, charge and discharge profiles of different cycles for the more representative cells for each cathode are reported in Fig. 7a. For all materials there is an evident polarization increment when current intensity is shifted from C/10 to C/5, which can also be seen from the wider overpotential  $\Delta E$  between discharge and charge curve. However, a comparison of the charge–discharge profiles for the different materials clearly highlights their distinct electrochemical behaviour, in agreement with the previously discussed results. In particular, the profiles of sample MX\_01 exhibit significantly higher polarization, clearly visible for the 5th cycle (C/5), where the second discharge plateau is completely absent. These evident differences among the four materials seem correlated with deposition kinetics reported before. dQ/dV curves were obtained from charge and discharge curves, in order to determine potentials at which electrochemical reactions occur and the overpotential ( $\Delta E$ ) between the second reduction peak

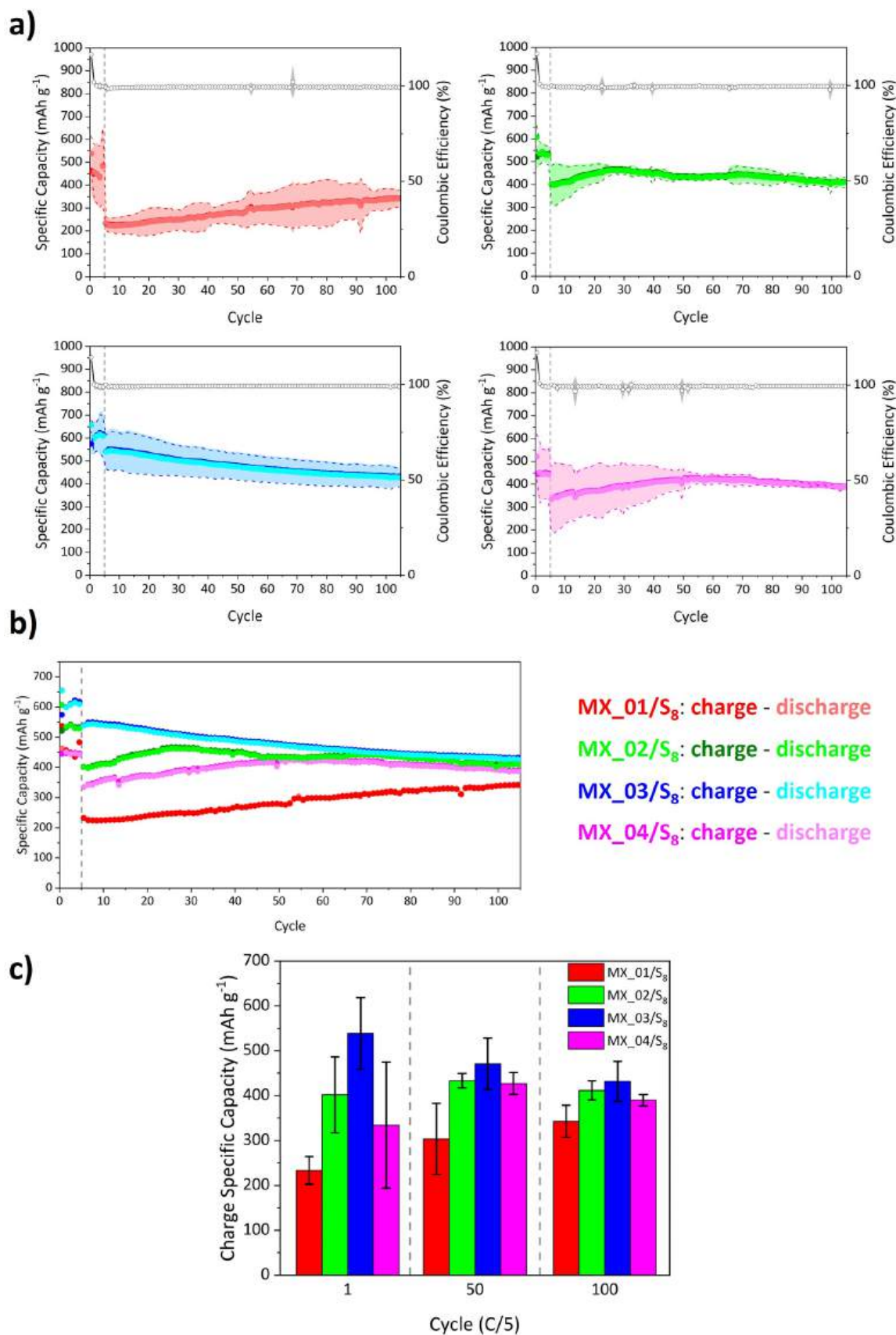


**Fig. 6.** a) Charge-discharge specific capacity and C.E. mean values with 95% confidence interval for sulphur composites obtained from each MXene sample b) Comparison between charge-discharge specific capacity mean values for composites obtained from each MXene sample c) Comparison between charge specific capacity mean values with associated confidence intervals for cycles 1, 50 and 100 at C/5 for each MXene sample.

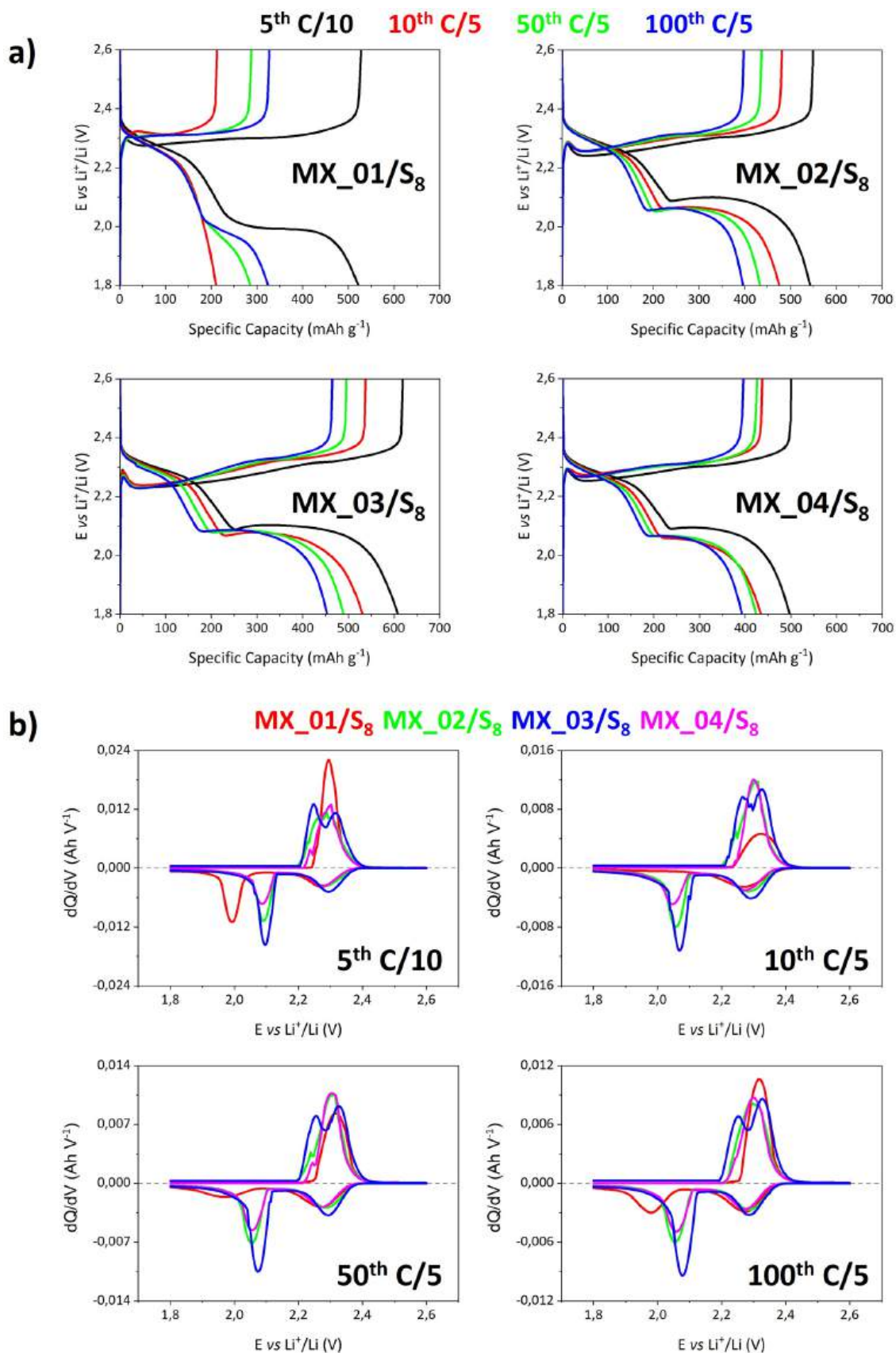


**Fig. 7.** a) Comparison between charge and discharge curves of the 5th cycle at C/10 and of cycles 10, 50 and 100 at C/5 for each MXene sample b) Comparison between dQ/dV curves derived from Figure 7 Fig. 7a charge-discharge curves for each MXene sample.

( $E_{R2}$ ) and the first oxidation peak ( $E_{O1}$ ). Fig. 7b shows that only sample MX\_03 is characterised by a well-defined double oxidation peak, indicating a more distinct potential separation for the charging process, which is coherent with the highest exchange current density observed in the anodic branch of Tafel plot for this sample. In the reduction process, all other samples show a slight shift of the first peak potential towards lower values. However, the most significant differences are associated with the peak corresponding to lithium sulphide deposition. More in detail, MX\_01 exhibits the most pronounced shift of the lithium sulphide deposition peak toward lower potentials already at C/10, while at C/5 the peak was not detectable and reappeared only after many cycle. In contrast, MX\_02 and MX\_04 show smaller, but still detectable, shifts together with lower peak intensities. Table 5 summarises peak potentials and  $\Delta E$  values for the fifth cycle at C/10 and the hundredth at C/5 of each sample. MX\_02 and MX\_03 samples showed lower overpotential than the other two MXenes.

The experimental and fitted results obtained from PEIS measurements conducted on MXene/sulphur composites-based fresh cells and after one discharge and charge cycle are reported as Nyquist plots in Figure S9 (a–d for “fresh cells”, e–h for “formed cells”), while the obtained resistances values, together with the total resistance, are reported in Table S5 for “fresh cells” and in Table S6 for “formed cells”, respectively. The equivalent circuits employed for experimental data fitting are, instead, displayed in Scheme S1.

For newly assembled cells, the equivalent circuit model adopted is the Randles circuit, composed of a resistance named  $R_{el}$ , which accounts for bulk electrolyte resistance, followed in series by first a constant phase element (CPE, a non-ideal capacitor) with a parallel resistance ( $C_{dl}/R_{ct}$ ) and then by an impedance element accounting for the semi-infinite diffusion process ( $W$ ).  $C_{dl}$  and  $R_{ct}$ , instead, represent electrical double-layer capacitance and charge transfer resistance at electrode/electrolyte interface, respectively.

For the impedance spectra obtained from the cells after the discharge–charge cycle, named as “formed”, a different equivalent circuit model was applied to perform data fitting with the addition of a second CPE in parallel with a resistance ( $C_{sulf}/R_{sulf}$ ) before the impedance element. This couple of parallel elements accounts for the small and distorted semicircle that appears at mid and low frequencies after the electrochemical activation of the sulphur/electrolyte interface, due to the low electrical conductivity of sulphur itself. The formation of this new interface just after one discharge and charge cycle could be linked to the high C.E. value (around 120%) observed for the first cycle. However, the appearance of a second semicircle in lithium-sulphur batteries impedance spectra is a commonly observed feature, also when C.E. values do not show deviations to the normal behaviour [74, 102]

By carefully analysing the obtained resistance values reported in the tables below, other interesting aspects can be observed for all the tested MXene samples. Right after cell assembly, bulk electrolyte resistance is comparable for all samples apart from MX\_04/S<sub>8</sub> composite, which shows a shifted value, probably due to cables and/or experimental setup influence. The charge transfer resistance, instead, slightly varies from 25.1 to 41.4  $\Omega$ . After the applied discharge and charge cycle, the studied

**Table 5**

Peak potential and overpotential values for cycle 5 at C/10 and 100 at C/10 derived from  $dQ/dV$  curves shown in Fig. 7b for each MXene sample.

Sample	Cycle	$E_{R1}$ (V)	$E_{R2}$ (V)	$E_{O1}$ (V)	$E_{O2}$ (V)	$\Delta E$ (mV)
MX_01/S <sub>8</sub>	5	2272	1991	2293	-	136
	100	2272	1978	2315	-	113
MX_02/S <sub>8</sub>	5	2282	2090	2289	-	57
	100	2287	2057	2292	-	73
MX_03/S <sub>8</sub>	5	2293	2096	2317	2248	73
	100	2286	2080	2327	2250	69
MX_04/S <sub>8</sub>	5	2274	2086	2302	-	83
	100	2273	2059	2298	-	93

systems vary consistently: apart from the already discussed appearance of a second semicircle in the impedance spectra, all the samples, apart from MX\_04/S<sub>8</sub> show an increased  $R_{el}$  value, in particular for sample MX\_01/S<sub>8</sub>. This can be either due to the consumption of different amounts of the electrolyte during the very first cycle or to a different amount of dissolved polysulphide species, which increase the electrolyte viscosity and, therefore, resistance.

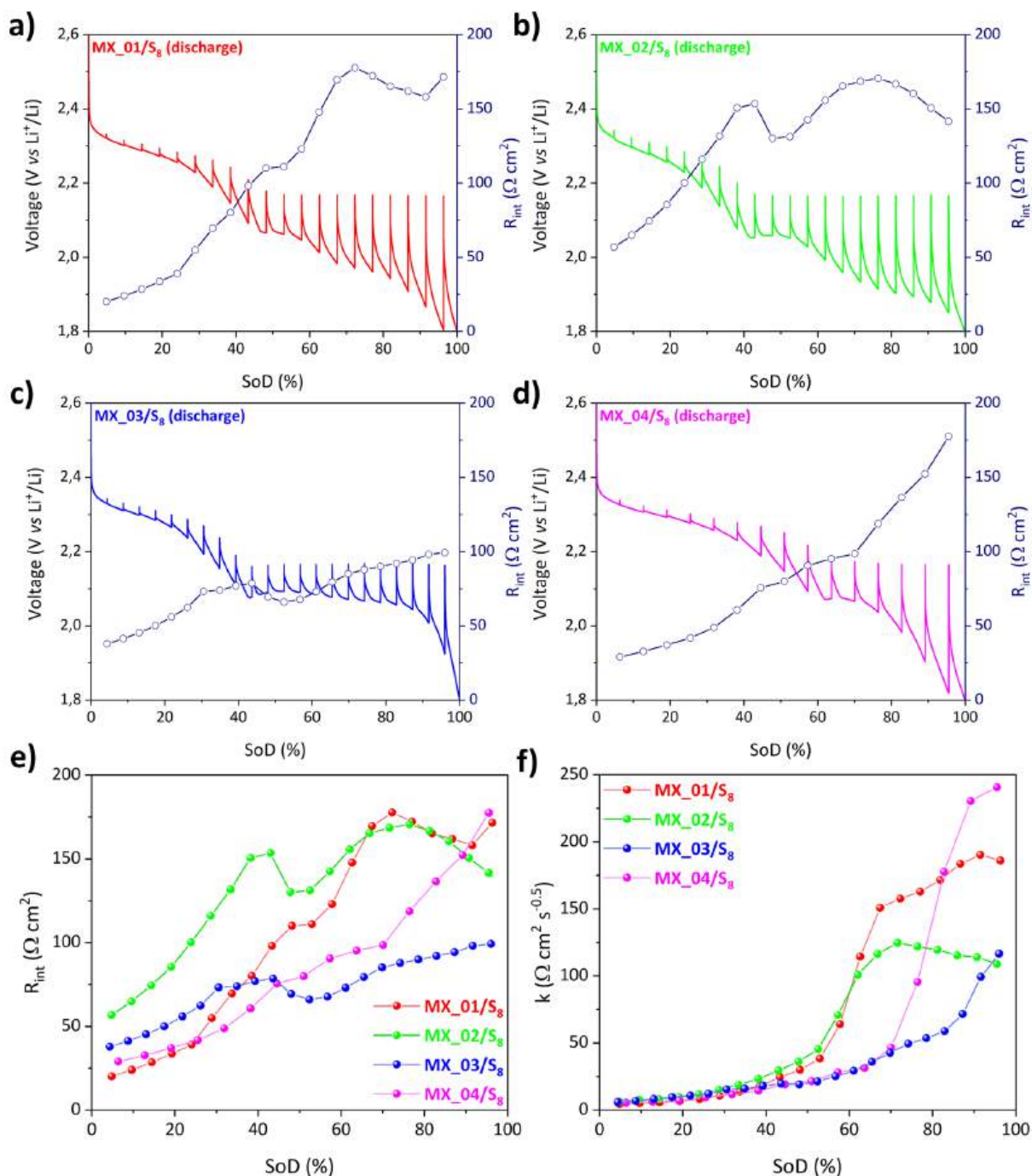
All  $R_{ct}$  values are significantly decreased after the first cycle, especially for sample MX\_03/S<sub>8</sub> with a reduction of around 87% if compared to the fresh cell, symptom of a significant activation process of the electrode/electrolyte interface after electrochemical reactions first occurred inside the cell. The resistance related to the sulphur/electrolyte interface  $R_{sulf}$ , instead, is below 6  $\Omega$  for all samples, with the lowest value for sample MX\_01/S<sub>8</sub>, probably because of its stronger interaction with sulphur and polysulphide species. However, after the first cycle, sample MX\_03/S<sub>8</sub> presents the lower total resistance.

Fig. 8 shows the results of the ICI test for each MXene/sulphur sample (8a–d) and the direct comparison between them of the extracted internal resistance ( $R_{int}$ , 8e) and the coefficient of diffusion resistance ( $k$ , 8f), which was demonstrated to be proportional to the coefficient of the Warburg impedance [76] Only results for the cell discharge are reported since it is the process where the main differences can be observed, while all tested samples behave similarly during the charging phase.

As can be seen, the evolution of the internal resistance during discharge presents a characteristic pattern with the lowest values at the beginning of the discharge, which then increases together with cell State of Discharge (SoD, %) reaching a local maximum coincident with the supersaturation point of the discharge curve. This is due to the increase in the electrolyte resistance because of lithium polysulphides dissolution, whose concentration reaches a peak in correspondence with the supersaturation point where the nucleation of Li<sub>2</sub>S starts. Then the internal cell resistance shows a slight decrease because of polysulphide species depletion from the electrolyte, with a successive new increase because of the insulating nature of the deposited Li<sub>2</sub>S solid phase. The entity of this low decrease and the new increase is highly dependent on the considered sample because of the different interactions with lithium polysulphides, together with Li<sub>2</sub>S deposition kinetics. In fact, sample MX\_03, which presented the fastest kinetics, is the one with the lowest increase in internal resistance both at the supersaturation point and during the second voltage plateau. Sample MX\_02, instead, has the highest  $R_{int}$  value from the beginning of the discharge, confirming the results obtained from PEIS analysis, but presents anyway a marked resistance reduction following Li<sub>2</sub>S nucleation thanks to its good deposition kinetics, with a subsequent internal resistance increase which leads to values comparable to other samples, apart from MX\_03, at the end of the discharge. This behaviour also seems coherent with the good performances shown by this sample in galvanostatic cycling after the “activation” period. For samples MX\_01 and MX\_04, instead, the local internal resistance maximum is less evident and more similar to a shoulder because of the lower Li<sub>2</sub>S deposition kinetics.

Considering the evolution of the coefficient of diffusion resistance  $k$  during discharge, instead, it is possible to note that lower and similar values among samples are characteristic for SoD values below 40%, while major differences are evident for higher SoD, corresponding to the second voltage plateau of the cell. Also for this parameter, the best performing sample is MX\_03, highlighting the importance of fast Li<sub>2</sub>S deposition kinetics on cell performance. At the end of the discharge, anyway, samples MX\_02 and MX\_03 present similar diffusion resistance values, while higher coefficients are obtained for the other two samples, consistent with their worse cell performances in galvanostatic cycling.

Based on the results of galvanostatic cycling, PEIS and ICI tests together with the analysis of the lithium sulphide deposition process and the evaluation of the catalytic effects of the different MXenes, sample MX\_03 was identified as the most promising candidate. Consequently, cells containing MX\_03 were subjected to extended cycling at C/5 for 500 cycles and directly compared to a reference cell using KJB/sulphur



**Fig. 8.** Results obtained for the ICI test performed on a) MX<sub>01</sub>/S<sub>8</sub> composite; b) MX<sub>02</sub>/S<sub>8</sub> composite; c) MX<sub>03</sub>/S<sub>8</sub> composite; d) MX<sub>04</sub>/S<sub>8</sub> composite; e) internal resistance evolution during discharge for each MXene/sulphur composite; f) coefficient of diffusion resistance evolution during discharge for each MXene/sulphur composite.

as the cathode material.

As reported in Fig. 9a, the MXene-based cell delivered a lower specific capacity (500 mAh g<sup>-1</sup>) during formation cycles if directly compared with KJB/sulphur cell (1000 ÷ 1100 mAh g<sup>-1</sup>). Nevertheless, in the subsequent cycles, the cell containing the MX<sub>03</sub>/sulphur cathode showed remarkable stability throughout the entire test at C/5, maintaining a specific capacity of 400 mAh g<sup>-1</sup> after 500 cycles. In contrast, KJB/sulphur reference cell underwent a drastic and continuous capacity decline over cycling. As expected, this rapid capacity fading led to the failure of the KJB/sulphur cell after just over 350 cycles, whereas the MXene-based cell remained active even after 500 cycles.

Fig. 9d reports the charge–discharge profiles for both MX<sub>03</sub>/S<sub>8</sub> and

KJB/S<sub>8</sub> cathodes, including the 1st and 5th formation cycles at C/10 (represented by dotted black and grey lines, respectively), the 10th cycle, and every 50th cycle at C/5 up to the end of the test for the MXene-based sulphur composite and until cell failure for the KJB-based cathode.

Focusing on the forming cycles at C/10, only in the case of MX<sub>03</sub> a consistent difference between the 1st and the 5th cycles is visible, consistent with what was previously discussed when comparing the four different MXene cathodes. In contrast, the KJB initial profiles are nearly overlapping, suggesting that the cell does not behave as if operating under lean-electrolyte conditions. This further supports the conclusion that the intrinsic differences between the host materials, especially

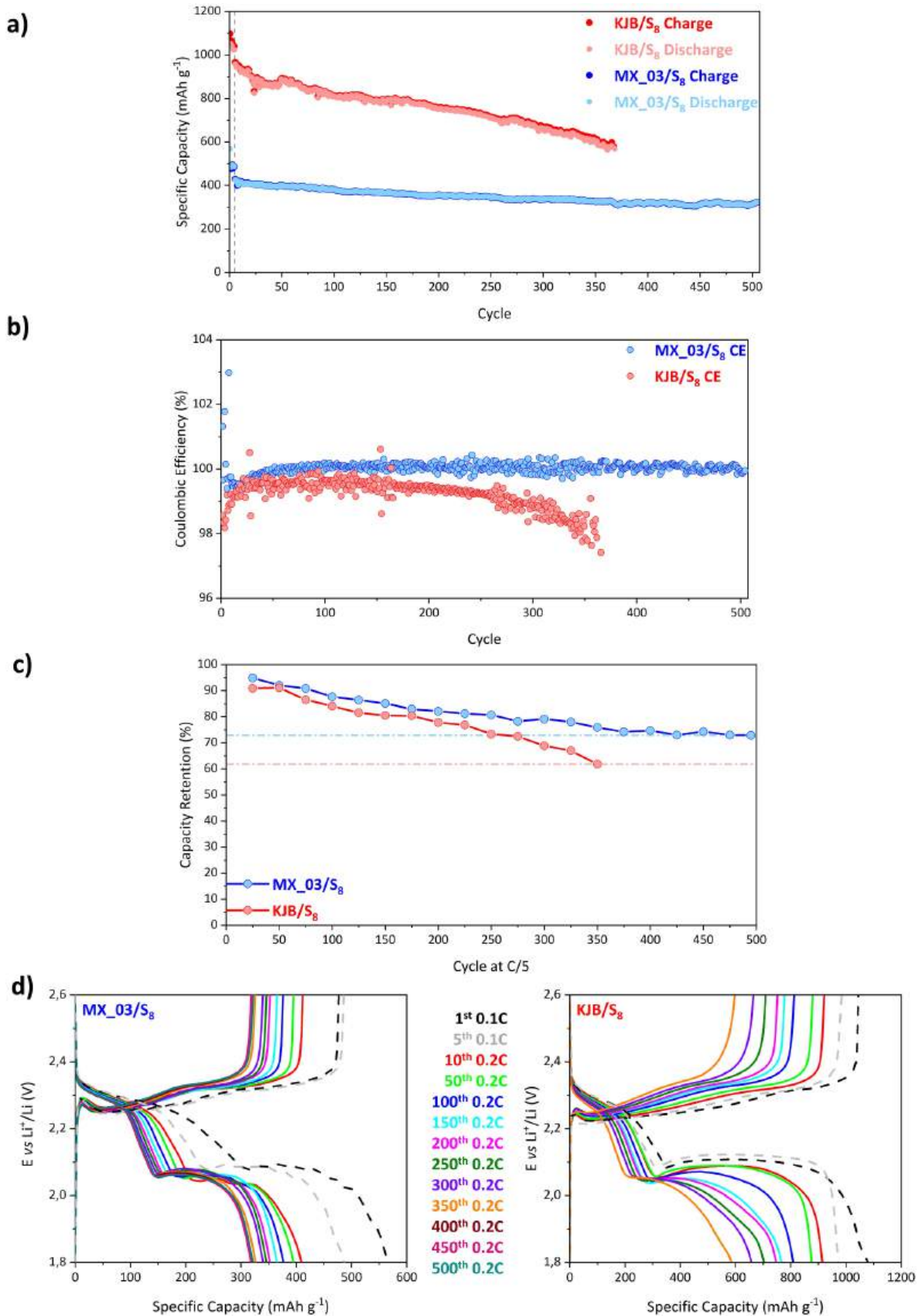


**Fig. 9.** a) Comparison between charge and discharge specific capacity values obtained from long cycling tests (5 cycles at C/10 + 500 at C/5) for KJB and MXene-containing sulphur composites; b) C.E. values calculated as discharge/charge specific capacities for cells presented in Figure 9a; c) Capacity retention calculated every 25 cycles at C/5 for MXene/sulphur and KJB/sulphur cathodes; d) Comparison between charge and discharge curves of the 1<sup>st</sup> and 5<sup>th</sup> cycle at C/10 (dotted lines) and of cycles 10, 50, 100, 150, 200, 250, 300, 350, 400, 450 and 500 at C/5 for MX\_03 and KJB containing sulphur composites.

porosity, have a significant impact on the final properties of the electrode and, consequently, on the overall performance of the cell.

After the C-rate increment, the MXene-based cell exhibits a greater loss in specific capacity compared to the KJB-based cell. This behaviour is mainly attributable to the lower conductivity. Despite this, the superior stability of the MXene/sulphur composite is also evident from the charge–discharge profiles. In fact, for MXene/sulphur cathode, the overall profile does not change significantly, especially after 200 cycles, and the  $\Delta E$  between charge and discharge curves seems almost constant. For KJB/sulphur cathode, instead, charge and discharge profiles undergo visible alteration during cycling and especially after 100 cycles with a growing  $\Delta E$  separation and the progressive loss of the second discharge plateau. This confirms that the strong interaction between MXene and sulphur, while limiting the full utilization of the active material specific capacity also because of the strong Ti–S bonds formation, enhances the reversibility of the redox process and significantly stabilises the electrochemical performance in terms of capacity retention during long-term cycling.

This hypothesis is also supported by Fig. 9b, where the C.E. values of KJB and MX\_03 sulphur cells are shown, and by Fig. 9c, which displays capacity retention for both types of lithium-sulphur cell at every 25 cycles at C/5. CE values for MXene/sulphur-based cells are stable, fluctuating between 99 and 100%, while the KJB/S cell shows a broader distribution of CE values, which progressively decline during cycling, dropping below 98% before cell failure. The evolution of capacity retention, evaluated considering charging steps and plotted every 25 cycles at C/5 in Fig. 9d, also confirms that using  $Ti_3C_2T_x$  MXenes as sulphur host enables to obtain higher stability: the final value after 500 cycles settles around 73% of the initial charge capacity at C/5, while using KJB as host a just 62% retention was found after 350 cycles, just before the cell end-of-life.

Furthermore, capacity fade of the two analysed sulphur hosts was also assessed by a linear regression of charge specific capacity values recorded every 25 cycles at C/5, as in both cases data show a pseudo-linear descending trend, as reported in Figure S10. Also, this kind of analysis agrees with the previous ones as the interpolated slope modulus for KJB/S<sub>8</sub> is almost four times the one obtained from  $Ti_3C_2$ -containing cell data, showing a higher rate of capacity decay.

#### 4. Conclusions

In this work, four different  $Ti_3C_2T_x$  MXenes were systematically studied as sulphur hosts for lithium-sulphur batteries with the specific aim of elucidating the role of the different etching conditions on polysulphides interaction and sulphur redox kinetics. By varying temperature, time and HF concentration, a series of  $Ti_3C_2T_x$  MXenes with comparable crystallographic structures, but distinct fluorinated and oxygenated content were obtained, allowing structural and chemical effects to be evaluated separately.

Electrochemical results showed that although the synthesis parameters were not changed drastically, clear differences are appreciable, where the extent of interaction with lithium polysulphide species and their conversion reaction kinetics, together with lithium sulphide deposition, are influenced by the slightly different morphological properties such as particle size distribution, *D*-spacing between planes in the material and surface functionalisation. In this case, a crucial role is attributed to the detected oxyfluoride species, in particular for sample MX\_03, which is obtained through a longer, but milder synthesis. Comprehensive physicochemical and electrochemical analyses demonstrate that the surface chemistry of MXenes critically regulates the balance between lithium polysulphide trapping and electrochemical conversion. In particular, Ti–F-rich surfaces exhibit strong polysulphide adsorption, effectively mitigating the shuttle effect, but it can hinder the nucleation of  $Li_2S$  and the overall electric conductivity. Conversely, MXenes with a more balanced surface environment promote faster sulphur reduction kinetics and more homogeneous  $Li_2S$  deposition.

The different properties also affect sulphur distribution and interaction after the melt diffusion process, with the formation of Ti–S stable bonds highlighted by XPS analysis. This strong interaction is crucial for the stabilisation of the cathodic material in the lithium-sulphur system, which in the case of MXene-based composite materials deliver stable specific capacity and C.E. values (> 99%) up to 500 cycles, with an extremely low capacity loss per cycle (< 0.27 mAh g<sup>-1</sup>), while a standard KJB/sulphur cathode showed a limited cell life of around 350 cycles with a higher capacity decay (> 1.15 mAh g<sup>-1</sup>).

Overall, this study supports the relationship between synthesis conditions, surface terminations, and electrochemical activity of  $Ti_3C_2T_x$  MXenes in lithium-sulphur batteries. Starting from these considerations, further studies could concentrate on the fine tuning and engineering of MXenes morphological and chemical properties to balance key factors such as lithium polysulphides adsorption, redox conversion kinetics, and lithium sulphide deposition, enabling better stability in Li-S systems.

#### Funding information

This work has not received any funding.

#### CRediT authorship contribution statement

**Leonardo Alberto Luciano:** Writing – original draft, Visualization, Methodology, Investigation, Data curation. **Tiziano Di Giulio:** Writing – original draft, Methodology, Investigation, Data curation. **Francesco Pellegrino:** Writing – review & editing, Validation, Supervision, Methodology, Conceptualization. **Roberto Colombo:** Methodology, Investigation. **Elisabetta Mazzotta:** Writing – review & editing, Validation, Resources, Methodology. **Cosimino Malitesta:** Writing – review & editing, Validation. **Valter Maurino:** Writing – review & editing, Resources. **Julia Amici:** Writing – review & editing, Validation, Resources, Methodology, Investigation. **Marco Minella:** Writing – review & editing, Validation, Supervision, Resources, Methodology, Conceptualization. **Daniele Versaci:** Writing – review & editing, Visualization, Validation, Supervision, Resources, Methodology, Conceptualization.

#### Declaration of competing interest

The authors declare that they have no known competing financial interests or personal relationships that could have appeared to influence the work reported in this paper.

#### Acknowledgments

FP, VM and MM acknowledge support from the Project CH4.0 under the MUR program "Dipartimenti di Eccellenza 2023–2027" (CUP: D13C22003520001).

#### Supplementary materials

Supplementary material associated with this article can be found, in the online version, at [doi:10.1016/j.ceja.2026.101260](https://doi.org/10.1016/j.ceja.2026.101260).

#### Data availability

Data will be made available on request.

#### References

- [1] F. Duffner, N. Kronmeyer, J. Tübke, J. Leker, M. Winter, R. Schmich, Post-lithium-ion battery cell production and its compatibility with lithium-ion cell production infrastructure, *Nature Energy* 6 (2021) 123–134, <https://doi.org/10.1038/s41560-020-00748-8>.
- [2] V.S. Kolosnitsyn, E.V. Karaseva, Lithium-sulfur batteries: problems and solutions, *Russ. J. Electrochem.* 44 (2008) 506–509, <https://doi.org/10.1134/S1023193508050029>.

- [3] B. Jin, J.U. Kim, H.B. Gu, Electrochemical properties of lithium–sulfur batteries, *J. Power. Sources*. 117 (2003) 148–152, [https://doi.org/10.1016/S0378-7753\(03\)00113-7](https://doi.org/10.1016/S0378-7753(03)00113-7).
- [4] X. Ji, L.F. Nazar, Advances in Li–S batteries, *J. Mater. Chem.* 20 (2010) 9821, <https://doi.org/10.1039/b925751a>.
- [5] Y.V. Mikhaylik, J.R. Akridge, Polysulfide shuttle study in the Li/S battery system, *J. Electrochem. Soc.* 151 (2004) A1969, <https://doi.org/10.1149/1.1806394>.
- [6] A.N. Mistry, P.P. Mukherjee, Shuttle in polysulfide Shuttle: friend or foe? *J. Phys. Chem. C* 122 (2018) 23845–23851, <https://doi.org/10.1021/ACS.JPC.8B06077>.
- [7] A. Bhargav, J. He, A. Gupta, A. Manthiram, Lithium–sulfur batteries: attaining the critical metrics, *Joule* 4 (2020) 285–291, <https://doi.org/10.1016/j.joule.2020.01.001>.
- [8] A. Manthiram, Y. Fu, S.H. Chung, C. Zu, Y.S. Su, Rechargeable lithium–Sulfur batteries, *Chem. Rev.* 114 (2014) 11751–11787, <https://doi.org/10.1021/cr500062v>.
- [9] L. Zhou, D.L. Danilov, F. Qiao, J. Wang, H. Li, R.A. Eichel, P.H.L. Notten, Sulfur reduction reaction in lithium–sulfur batteries: mechanisms, catalysts, and characterization, *Adv. Energy Mater.* 12 (2022) 2202094, <https://doi.org/10.1002/AENM.202202094>.
- [10] M. Sawangphruk, New materials for lithium–sulfur batteries: challenges and future directions, *Chem. Commun.* 61 (2025) 7770–7794, <https://doi.org/10.1039/D5CC01150G>.
- [11] M.R. Krishnan, C.S. Bongu, E.H. Alsharaeh, Recent developments and prospects on functional graphene-based nanocomposites as potential sulfur hosts for next-generation lithium–sulfur batteries, *Energy Environ. Mater.* 8 (2025) e70032, <https://doi.org/10.1002/EEM2.70032>.
- [12] Y. Min, X. Zou, Q. Lu, W. Cai, Y. Bu, Advances in the catalytic mechanism of metal oxides for lithium–Sulfur batteries, *Small* 21 (2025) 2411794, <https://doi.org/10.1002/SMLL.202411794>.
- [13] Y. Xiao, C. Qi, D. Yang, D. Ma, S. Huang, Toward high performance lithium–sulfur batteries based on metal–organic frameworks: progress and prospects, *Mater. Sci. Eng.*, B 313 (2025) 117983, <https://doi.org/10.1016/J.MSEB.2025.117983>.
- [14] X. Chen, H. Jiang, J.H. Liu, H. Zhang, C. Zhan, Y. Gao, X. Jiang, Y. Wang, X. Cao, S.L. Chou, Covalent organic frameworks and their derivatives for applications in high-performance lithium–Sulfur batteries, *Adv. Funct. Mater.* 35 (2025) 2421697, <https://doi.org/10.1002/ADFM.202421697>.
- [15] Q. Guan, Q. Zhuang, W. Xu, Y. Zhang, S. Cheng, J. Zhang, M. Liu, H. Lin, J. Wang, Accelerated kinetics of desolvation and redox transformation enabled by MOF sieving for high-loading Mg–S battery, *Adv. Funct. Mater.* 35 (2025) 2506397, <https://doi.org/10.1002/ADFM.202506397>.
- [16] P. Zeng, G. Li, X. Zhao, Y. Wan, B. Huang, X. Huang, J. Peng, M. Chen, X. Wang, Construction and catalysis role of a kinetic promoter based on lithium–insertion technology and proton exchange strategy for lithium–sulfur batteries, *J. Colloid. Interface Sci.* 670 (2024) 519–529, <https://doi.org/10.1016/J.JCIS.2024.05.123>.
- [17] P. Zeng, K. Miao, H. Zhang, G. Xiang, M. Chen, X. Wang, Synergistic catalysis of VN quantum dots and S/N heteroatoms enabling fast reaction kinetics for lithium–sulfur batteries, *Chem. Commun.* 61 (2025) 14991–14994, <https://doi.org/10.1039/D5CC04053A>.
- [18] H. Zhang, P. Zeng, X. Zhao, B. Huang, X. Wang, Surface reconstruction for a spinel-type electrocatalyst towards fast sulfur conversion in advanced lithium–sulfur batteries, *Chem. Eng. J.* 513 (2025) 162806, <https://doi.org/10.1016/J.CEJ.2025.162806>.
- [19] X. Li, Z. Huang, C.E. Shuck, G. Liang, Y. Gogotsi, C. Zhi, MXene chemistry, electrochemistry and energy storage applications, *Nat. Rev. Chem.* 6 (2022) 389–404, <https://doi.org/10.1038/s41570-022-00384-8>, 6, 6.
- [20] M. Naguib, V.N. Mochalin, M.W. Barsoum, Y. Gogotsi, M. Naguib, V.N. Mochalin, M.W. Barsoum, Y. Gogotsi, 25th anniversary article: MXenes: a new family of two-dimensional materials, *Adv. Mater.* 26 (2014) 992–1005, <https://doi.org/10.1002/ADMA.201304138>.
- [21] M. Naguib, M. Kurtoglu, V. Presser, J. Lu, J. Niu, M. Heon, L. Hultman, Y. Gogotsi, M.W. Barsoum, Two-dimensional nanocrystals produced by exfoliation of Ti<sub>3</sub>AlC<sub>2</sub>, *Adv. Mater.* 23 (2011) 4248–4253, <https://doi.org/10.1002/ADMA.201102306>.
- [22] M. Jiang, D. Wang, Y.H. Kim, C. Duan, D.V. Talapin, C. Zhou, Evolution of surface chemistry in two-dimensional MXenes: from mixed to tunable uniform terminations, *Angew. Chem., Int. Ed.* 63 (2024) e202409480, <https://doi.org/10.1002/ANIE.202409480>.
- [23] X. Liang, A. Garsuch, L.F. Nazar, Sulfur cathodes based on conductive MXene nanosheets for high-performance lithium–Sulfur batteries, *Angew. Chem., Int. Ed.* 54 (2015) 3907–3911, <https://doi.org/10.1002/ANIE.201410174>.
- [24] X. Liang, Y. Rangom, C.Y. Kwok, Q. Pang, L.F. Nazar, X. Liang, Y. Rangom, C. Y. Kwok, Q. Pang, L.F. Nazar, Interwoven MXene nanosheet/carbon-nanotube composites as Li–S cathode hosts, *Adv. Mater.* 29 (2017) 1603040, <https://doi.org/10.1002/ADMA.201603040>.
- [25] X. Liang, C. Hart, Q. Pang, A. Garsuch, T. Weiss, L.F. Nazar, A highly efficient polysulfide mediator for lithium–sulfur batteries, *Nat. Commun.* 6 (2015) 20151–8, <https://doi.org/10.1038/ncomms56682>, 1, 6.
- [26] Q. Zhao, Q. Zhu, Y. Liu, B. Xu, Q. Zhao, Y. Liu, Q. Zhu, B. Xu, Status and prospects of MXene-based lithium–Sulfur batteries, *Adv. Funct. Mater.* 31 (2021) 2100457, <https://doi.org/10.1002/ADFM.202100457>.
- [27] T. Boteju, S. Ponnuram, V. Thangadurai, MXenes as effective sulfur hosts and electrocatalysts to suppress lithium polysulfide shuttling: a computational study, *J. Phys. Chem. C* 128 (2024) 3652–3661, <https://doi.org/10.1021/acs.jpcc.3c07776>.
- [28] S. Saharan, U. Ghanekar, S. Meena, Two-dimensional MXenes for energy storage: computational and experimental approaches, *ChemistrySelect*. 7 (2022) e202203288, <https://doi.org/10.1002/SLCT.202203288>.
- [29] B. Anasori, M. Naguib, Two-dimensional MXenes, *MRS Bull.* 48 (2023) 238–244, <https://doi.org/10.1557/s43577-023-00500-z>.
- [30] X. Geng, L. Yang, P. Song, Application of MXene-based materials for cathode in lithium–sulfur batteries, *Chem. Eur. J.* 30 (2024) e202303451, <https://doi.org/10.1002/CHEM.202303451>.
- [31] T. Zhao, P. Zhai, Z. Yang, J. Wang, L. Qu, F. Du, J. Wang, Self-supporting Ti<sub>3</sub>C<sub>2</sub>T<sub>x</sub> foam/S cathodes with high sulfur loading for high-energy-density lithium–sulfur batteries, *Nanoscale* 10 (2018) 22954–22962, <https://doi.org/10.1039/C8NR08642G>.
- [32] H. Zhang, Y. Wang, Y. Sun, P. Huang, Layered structure Ti<sub>3</sub>C<sub>2</sub> MXene as a functional catalyst for advanced electrochemical performance, *Ionics (Kiel)* 28 (2022) 3957–3961, <https://doi.org/10.1007/s11581-022-04619-y>.
- [33] X. Zhao, M. Liu, Y. Chen, B. Hou, N. Zhang, B. Chen, N. Yang, K. Chen, J. Li, L. An, Fabrication of layered Ti<sub>3</sub>C<sub>2</sub> with an accordion-like structure as a potential cathode material for high performance lithium–sulfur batteries, *J. Mater. Chem. Mater.* 3 (2015) 7870–7876, <https://doi.org/10.1039/C4TA07101H>.
- [34] W. Bao, X. Xie, J. Xu, X. Guo, J. Song, W. Wu, D. Su, G. Wang, Confined sulfur in 3D MXene/reduced graphene oxide hybrid nanosheets for lithium–Sulfur battery, *Chem. - Eur. J.* 23 (2017) 12613–12619, <https://doi.org/10.1002/CHEM.201702387>.
- [35] X. Liang, Y. Rangom, C.Y. Kwok, Q. Pang, L.F. Nazar, Interwoven MXene nanosheet/carbon-nanotube composites as Li–S cathode hosts, *Adv. Mater.* 29 (2017), <https://doi.org/10.1002/ADMA.201603040>.
- [36] R. Gan, N. Yang, Q. Dong, N. Fu, R. Wu, C. Li, Q. Liao, J. Li, Z. Wei, Enveloping ultrathin Ti<sub>3</sub>C<sub>2</sub> nanosheets on carbon fibers: a high-density sulfur loaded lithium–sulfur battery cathode with remarkable cycling stability, *J. Mater. Chem. Mater.* 8 (2020) 7253–7260, <https://doi.org/10.1039/D0TA02374D>.
- [37] Y. Zhang, W. Tang, R. Zhan, H. Liu, H. Chen, J. Yang, M. Xu, An N-doped porous carbon/MXene composite as a sulfur host for lithium–sulfur batteries, *Inorg. Chem. Front.* 6 (2019) 2894–2899, <https://doi.org/10.1039/C9QI00723G>.
- [38] J. Wang, T. Zhao, Z. Yang, Y. Chen, Y. Liu, J. Wang, P. Zhai, W. Wu, MXene-based Co, N-codoped porous carbon nanosheets regulating polysulfides for high-performance lithium–sulfur batteries, *ACS. Appl. Mater. Interfaces* 11 (2019) 38654–38662, <https://doi.org/10.1021/ACSAMI.9B11988>.
- [39] H. Pan, X. Huang, R. Zhang, D. Wang, Y. Chen, X. Duan, G. Wen, Titanium oxide–Ti<sub>3</sub>C<sub>2</sub> hybrids as sulfur hosts in lithium–sulfur battery: fast oxidation treatment and enhanced polysulfide adsorption ability, *Chem. Eng. J.* 358 (2019) 1253–1261, <https://doi.org/10.1016/J.CEJ.2018.10.026>.
- [40] H. Zhang, Q. Qi, P. Zhang, W. Zheng, J. Chen, A. Zhou, W. Tian, W. Zhang, Z. Sun, Self-assembled 3D MnO<sub>2</sub> nanosheets/delaminated-Ti<sub>3</sub>C<sub>2</sub> aerogel as sulfur host for lithium–Sulfur battery cathodes, *ACS. Appl. Energy Mater.* 2 (2019) 705–714, <https://doi.org/10.1021/acsaem.8b01765>.
- [41] C. Du, J. Wu, P. Yang, S. Li, J. Xu, K. Song, Embedding S@TiO<sub>2</sub> nanospheres into MXene layers as high rate cyclability cathodes for lithium–sulfur batteries, *Electrochim. Acta* 295 (2019) 1067–1074, <https://doi.org/10.1016/J.ELECTACTA.2018.11.143>.
- [42] V.P. Nguyen, J.S. Park, H.C. Shim, J.M. Yuk, J.H. Kim, D. Kim, S.M. Lee, V. P. Nguyen, H.C. Shim, J.H. Kim, S.M. Lee, J.S. Park, J.M. Yuk, D. Kim, Accelerated sulfur evolution reactions by Ti<sub>2</sub>/TiO<sub>2</sub>@MXene host for high-volumetric-energy-density lithium–Sulfur batteries, *Adv. Funct. Mater.* 33 (2023) 2303503, <https://doi.org/10.1002/ADFM.202303503>.
- [43] J. Guo, H. Chen, D. Wang, W. Liu, G. Huang, X. Zhang, Iterative design of polymer fabric cathode for metal-ion batteries, *Sci. Bull. (Beijing)* 69 (2024) 3237–3246, <https://doi.org/10.1016/J.SCI.2024.08.010>.
- [44] Y. Dong, S. Zheng, J. Qin, X. Zhao, H. Shi, X. Wang, J. Chen, Z.S. Wu, All-MXene-based integrated electrode constructed by Ti<sub>3</sub>C<sub>2</sub> nanoribbon framework host and nanosheet interlayer for high-energy-density Li–S batteries, *ACS. Nano* 12 (2018) 2381–2388, <https://doi.org/10.1021/ACS.NANO.7B07672>.
- [45] J. Song, D. Su, X. Xie, X. Guo, W. Bao, G. Shao, G. Wang, Immobilizing polysulfides with MXene-functionalized separators for stable lithium–sulfur batteries, *ACS. Appl. Mater. Interfaces* 8 (2016) 29427–29433, <https://doi.org/10.1021/ACSAMI.6B09027>.
- [46] N. Li, W. Cao, Y. Liu, H. Ye, K. Han, Impeding polysulfide shuttling with a three-dimensional conductive carbon nanotubes/MXene framework modified separator for highly efficient lithium–sulfur batteries, *Colloids. Surf. Physicochem. Eng. Asp.* 573 (2019) 128–136, <https://doi.org/10.1016/J.COLSURFA.2019.04.054>.
- [47] Z.U. Rehman, K. Khan, S. Yao, M. Nawaz, A. Miotello, M.A. Assiri, T. Bashir, T. L. Tamang, M.S. Javed, Recent progress in MXene-based materials, synthesis, design, and application in lithium–sulfur batteries, *Mater. Today Chem.* 40 (2024) 102200, <https://doi.org/10.1016/J.MTCH.2024.102200>.
- [48] Y. Bi, S. Tian, Y. Zhang, A. Huang, P. Kumar, Z. Ma, W. Liu, J. Ming, Helmholtz plane engineering enables dendrite-free and subzero-stable aqueous Zn batteries, *ACS. Energy Lett.* 11 (2026) 1670–1679, <https://doi.org/10.1021/acsenenergylett.5c03049>.
- [49] Y. Zhang, Z. Hu, Y. Bi, S. Tian, H. Sun, K. Li, W. Liu, L. Sun, W. Liu, D. Wang, Cold-pressing strategy for constructing simple and high-performance dendrite-free zinc anodes for aqueous zinc-ion batteries, *ACS. Sustain. Chem. Eng.* 13 (2025) 5381–5393, <https://doi.org/10.1021/acssuschemeng.5c00832>.
- [50] Z. Yan, J. Zhu, Y. Wan, P. Zeng, Kinetics enhancement of an advanced separator modified by vanadium-based MXene for Li–S batteries, *Mater. Lett.* 375 (2024) 137238, <https://doi.org/10.1016/J.MATLET.2024.137238>.
- [51] S. Wu, X. Li, Y. Zhang, Q. Guan, J. Wang, C. Shen, H. Lin, J. Wang, Y. Wang, L. Zhan, L. Ling, Interface engineering of MXene-based heterostructures for

- lithium-sulfur batteries, *Nano Res.* 16 (2023) 9158–9178, <https://doi.org/10.1007/s12274-023-5532-2>.
- [52] X. Li, Y. Zuo, Y. Zhang, J. Wang, Y. Wang, H. Yu, L. Zhan, L. Ling, Z. Du, S. Yang, Controllable sulfuration of MXenes to In-plane multi-heterostructures for efficient sulfur redox kinetics, *Adv. Energy Mater.* 14 (2024) 2303389, <https://doi.org/10.1002/AENM.202303389>.
- [53] Y. Li, Y. Zuo, X. Li, Y. Zhang, C. Ma, X. Cheng, J. Wang, J. Wang, H. Lin, L. Ling, Electron delocalization-enhanced sulfur reduction kinetics on an MXene-derived heterostructured electrocatalyst, *Nano Res.* 17 (2024) 7153–7162, <https://doi.org/10.1007/s12274-024-6682-6>.
- [54] J. Bao, X. Li, T. Rong, J. Wang, J. Gu, X. Cheng, Y. Wang, H. Lin, L. Cheng, L. Zhan, Y. Zhang, Single atomic Co decorated mesoporous carbon/MXene heterostructure as redox promoters for high-stable Li-S battery, *Carbon*. N. Y. 238 (2025) 120229, <https://doi.org/10.1016/J.CARBON.2025.120229>.
- [55] G. Deng, G. Tang, W. Xi, Y. Zhang, D. Cai, R. Wang, Y. Gong, B. He, H. Wang, J. Jin, 3D-printed Co-doped MoS<sub>2</sub>/Ti<sub>3</sub>C<sub>2</sub>Tx/S cathode with accelerated adsorption and conversion of lithium polysulfides for advanced lithium-sulfur batteries, *Mater. Today Energy* 51 (2025) 101877, <https://doi.org/10.1016/J.MTENER.2025.101877>.
- [56] L. Chen, X. Chen, J. Xiao, Flower-like Ti<sub>3</sub>C<sub>2</sub>Tx-TiO<sub>2</sub> modified with ZnS nanoparticles as adsorption-catalytic cathodic material for lithium-sulfur batteries, *J. Energy Storage* 118 (2025) 116241, <https://doi.org/10.1016/J.EST.2025.116241>.
- [57] G. Deng, Z. Jiang, G. Tang, W. Xi, Y. Zhang, S. Huang, D. Cai, R. Wang, Y. Gong, H. Wang, J. Jin, MXene/SnS Mott-Schottky heterostructure for modulation of sulfur reduction reaction kinetics in advanced lithium-sulfur batteries, *J. Energy Chem.* 110 (2025) 19–28, <https://doi.org/10.1016/J.JEACHEM.2025.06.033>.
- [58] T. Li, C. Yang, H. Hao, Z. Yuan, Z. Yu, H. Liu, MXene porous engineering as lithium-ion kinetic pump for durable lithium-sulfur batteries, *J. Alloys. Compd.* 1022 (2025) 180032, <https://doi.org/10.1016/J.JALLCOM.2025.180032>.
- [59] K. Guan, X. Li, Q. Xie, L. Huang, H. Zhang, G. Li, W. Lei, Hierarchical Co-doped hollow Ti<sub>3</sub>C<sub>2</sub>Tx tubes with built-in electron/ion transport network for high-performance lithium sulfur batteries, *Chem. Eng. J.* 492 (2024) 151978, <https://doi.org/10.1016/J.CEJ.2024.151978>.
- [60] R. Liu, S. Zhai, Z. Ye, M. Liu, Y. Xu, C. Li, X. Wang, T. Mei, Constructing carbon nanotube-optimized hollow Ti<sub>3</sub>C<sub>2</sub> MXene hierarchical conductive networks for robust lithium-sulfur batteries, *J. Mater. Chem. Mater.* 11 (2023) 24330–24337, <https://doi.org/10.1039/D3TA04677J>.
- [61] T. Zeng, R. Chen, K. Chen, M. Tang, Z. Xiao, Y. Wang, J. Shen, B. Jin, Electrostatic self-assembly mxene@biomass porous carbon with superior cycle stability for lithium-sulfur batteries, *Mater. Chem. Phys.* 293 (2023) 126874, <https://doi.org/10.1016/J.MATCHEMPHYS.2022.126874>.
- [62] K. Qi, F. Zhang, Rational surface engineering of Ti<sub>3</sub>C<sub>2</sub>Tx MXene for high-performance lithium-sulfur batteries, *Mater. Lett.* 318 (2022) 132134, <https://doi.org/10.1016/J.MATLET.2022.132134>.
- [63] T. Zhang, W. Shao, S. Liu, Z. Song, R. Mao, X. Jin, X. Jian, F. Hu, A flexible design strategy to modify Ti<sub>3</sub>C<sub>2</sub>Tx MXene surface terminations via nucleophilic substitution for long-life Li-S batteries, *J. Energy Chem.* 74 (2022) 349–358, <https://doi.org/10.1016/J.JEACHEM.2022.07.041>.
- [64] T. Wang, D. Luo, Y. Zhang, Z. Zhang, J. Wang, G. Cui, X. Wang, A. Yu, Z. Chen, Hierarchically porous Ti<sub>3</sub>C<sub>2</sub> MXene with tunable active edges and unsaturated coordination bonds for superior lithium-sulfur batteries, *ACS. Nano* 15 (2021) 19457–19467, <https://doi.org/10.1021/acsnano.1c06213>.
- [65] C. Wen, X. Zheng, X. Li, M. Yuan, H. Li, G. Sun, Rational design of 3D hierarchical MXene@AlF<sub>3</sub>/Ni(OH)<sub>2</sub> nanohybrid for high-performance lithium-sulfur batteries, *Chem. Eng. J.* 409 (2021) 128102, <https://doi.org/10.1016/J.CEJ.2020.128102>.
- [66] H. Chen, G. Ke, X. Wu, W. Li, Y. Li, H. Mi, L. Sun, Q. Zhang, C. He, X. Ren, Amorphous MoS<sub>3</sub> decoration on 2D functionalized MXene as a bifunctional electrode for stable and robust lithium storage, *Chem. Eng. J.* 406 (2021) 126775, <https://doi.org/10.1016/J.CEJ.2020.126775>.
- [67] H. Pan, X. Huang, R. Zhang, D. Wang, Y. Chen, X. Duan, G. Wen, Titanium oxide-Ti<sub>3</sub>C<sub>2</sub> hybrids as sulfur hosts in lithium-sulfur battery: fast oxidation treatment and enhanced polysulfide adsorption ability, *Chem. Eng. J.* 358 (2019) 1253–1261, <https://doi.org/10.1016/J.CEJ.2018.10.026>.
- [68] X. Zhao, M. Liu, Y. Chen, B. Hou, N. Zhang, B. Chen, N. Yang, K. Chen, J. Li, L. An, Fabrication of layered Ti<sub>3</sub>C<sub>2</sub> with an accordion-like structure as a potential cathode material for high performance lithium-sulfur batteries, *J. Mater. Chem. Mater.* 3 (2015) 7870–7876, <https://doi.org/10.1039/C4TA07101H>.
- [69] V. Natu, M. Benchakar, C. Canaff, A. Habrioux, S. Célérier, M.W. Barsoum, A critical analysis of the X-ray photoelectron spectra of Ti<sub>3</sub>C<sub>2</sub>Tz MXenes, *Matter* 4 (2021) 1224–1251, <https://doi.org/10.1016/J.MATT.2021.01.015>.
- [70] Y. Lu, D. Li, F. Liu, Characterizing the chemical structure of Ti<sub>3</sub>C<sub>2</sub>Tx MXene by angle-resolved XPS combined with argon ion etching, *Materials (Basel)* 15 (2022) (2022) 307, <https://doi.org/10.3390/MA15010307>, 15.
- [71] K. Maleski, C.E. Ren, M. Q. Zhao, B. Anasori, Y. Gogotsi, Size-dependent physical and electrochemical properties of two-dimensional MXene flakes, *ACS. Appl. Mater. Interfaces* 10 (2018) 24491–24498, <https://doi.org/10.1021/acsami.8b04662>.
- [72] T.D. Papanasiou, A. Tsiantis, Y. Wang, Obtaining the dimensions and orientation of 2D rectangular flakes from sectioning experiments in flake composites, *J. Compos. Sci.* 6 (2022) (2022) 142, <https://doi.org/10.3390/JCS6050142>.
- [73] N.L. Le, S. L. Hsu, T.H. Vu, C. Y. Liu, Q.H. Dinh, A. Arya, E.Y. T. Li, Y. S. Su, Transformation of polysulfide catholyte chemistry through lithium-arene complexes for superior solubility and cyclability in Li-S batteries, *JACS. Au* 5 (2025) 3866–3878, <https://doi.org/10.1021/jacsau.5c00537>.
- [74] N.A. Cañas, K. Hirose, B. Pascucci, N. Wagner, K.A. Friedrich, R. Hiesgen, Investigations of lithium-sulfur batteries using electrochemical impedance spectroscopy, *Electrochim. Acta* 97 (2013) 42–51, <https://doi.org/10.1016/J.ELECTACTA.2013.02.101>.
- [75] M.J. Lacey, Influence of the electrolyte on the internal resistance of lithium-sulfur batteries studied with an intermittent current interruption method, *ChemElectroChem.* 4 (2017) 1997–2004, <https://doi.org/10.1002/CELCC.201700129>.
- [76] Y. C. Chien, A.S. Menon, W.R. Brant, D. Brandell, M.J. Lacey, Simultaneous monitoring of crystalline active materials and resistance evolution in lithium-sulfur batteries, *J. Am. Chem. Soc.* 142 (2020) 1449–1456, <https://doi.org/10.1021/jacs.9b11500>.
- [77] A. Primieri, R. Santalucia, E. Alladio, E. Corrao, M. Isola, F. Pellegrino, V. Maurino, Innovative approaches to safe and sustainable material synthesis: optimizing Ti<sub>3</sub>C<sub>2</sub> MXene properties via design of experiments and chemometric analysis, *Green Anal. Chem.* 13 (2025) 100264, <https://doi.org/10.1016/J.GREEAC.2025.100264>.
- [78] M. Shekhirev, C.E. Shuck, A. Sarycheva, Y. Gogotsi, Characterization of MXenes at every step, from their precursors to single flakes and assembled films, *Prog. Mater. Sci.* 120 (2021) 100757, <https://doi.org/10.1016/J.PMATSCI.2020.100757>.
- [79] P.O.Å. Persson, J. Rosen, Current state of the art on tailoring the MXene composition, structure, and surface chemistry, *Curr. Opin. Solid. State Mater. Sci.* 23 (2019) 100774, <https://doi.org/10.1016/J.COSSMS.2019.100774>.
- [80] J. Halim, M.R. Lukatskaya, K.M. Cook, J. Lu, C.R. Smith, L. Å. Näslund, S.J. May, L. Hultman, Y. Gogotsi, P. Eklund, M.W. Barsoum, Transparent conductive two-dimensional titanium carbide epitaxial thin films, *Chem. Mater.* 26 (2014) 2374–2381, <https://doi.org/10.1021/cm500641a>.
- [81] Q. Gu, Y. Cao, J. Chen, Y. Qi, Z. Zhai, M. Lu, N. Huang, B. Zhang, Fluorine-modulated MXene-derived catalysts for multiphase sulfur conversion in lithium-sulfur battery, *Nanomicro Lett.* 16 (2024) 266, <https://doi.org/10.1007/s40820-024-01482-6>.
- [82] L.H. Karlsson, J. Birch, J. Halim, M.W. Barsoum, P.O.Å. Persson, Atomically resolved structural and chemical investigation of single MXene sheets, *Nano Lett.* 15 (2015) 4955–4960, <https://doi.org/10.1021/acs.nanolett.5b00737>.
- [83] V. Natu, M. Benchakar, C. Canaff, A. Habrioux, S. Célérier, M.W. Barsoum, A critical analysis of the X-ray photoelectron spectra of Ti<sub>3</sub>C<sub>2</sub>Tz MXenes, *Matter* 4 (2021) 1224–1251, <https://doi.org/10.1016/J.MATT.2021.01.015>.
- [84] L. Å. Näslund, P.O.Å. Persson, J. Rosen, X-ray photoelectron spectroscopy of Ti<sub>3</sub>AlC<sub>2</sub>, Ti<sub>3</sub>C<sub>2</sub>T<sub>z</sub>, and TiC provides evidence for the electrostatic interaction between laminated layers in MAX-phase materials, *J. Phys. Chem. C* 124 (2020) 27732–27742, <https://doi.org/10.1021/acs.jpcc.0c07413>.
- [85] M. Mićušić, M. Šlouf, A. Stepura, Y. Soyka, E. Ovodok, M. Procházka, M. Omastová, Aging of 2D MXene nanoparticles in air: an XPS and TEM study, *Appl. Surf. Sci.* 610 (2023) 155351, <https://doi.org/10.1016/J.APSUSC.2022.155351>.
- [86] J. Häcker, D.H. Nguyen, T. Rommel, Z. Zhao-Karger, N. Wagner, K.A. Friedrich, Operando UV/vis spectroscopy providing insights into the sulfur and polysulfide dissolution in magnesium-Sulfur batteries, *ACS. Energy Lett.* 7 (2022) 1–9, <https://doi.org/10.1021/acsenergylett.1c02152>.
- [87] D.S. Wu, F. Shi, G. Zhou, C. Zu, C. Liu, K. Liu, Y. Liu, J. Wang, Y. Peng, Y. Cui, Quantitative investigation of polysulfide adsorption capability of candidate materials for Li-S batteries, *Energy Storage Mater.* 13 (2018) 241–246, <https://doi.org/10.1016/J.ENSMS.2018.01.020>.
- [88] R. Colombo, D. Versaci, J. Amici, F. Bella, M.L. Para, N. Garino, M. Laurenti, S. Bodoardo, C. Francia, Reduced graphene oxide embedded with ZnS nanoparticles as catalytic cathodic material for Li-S batteries, *Nanomaterials* 13 (2023) 2149, <https://doi.org/10.3390/NANO13142149/S1>.
- [89] R. Hou, S. Zhang, P. Zhang, Y. Zhang, X. Zhang, N. Li, Z. Shi, G. Shao, Ti<sub>3</sub>C<sub>2</sub> MXene as an “energy band bridge” to regulate the heterointerface mass transfer and electron reversible exchange process for Li-S batteries, *J. Mater. Chem. Mater.* 8 (2020) 25255–25267, <https://doi.org/10.1039/D0TA06695H>.
- [90] A. Bewick, M. Fleischmann, H.R. Thirsk, Kinetics of the electrocrystallization of thin films of calomel, *Trans. Faraday Soc.* 58 (1962) 2200, <https://doi.org/10.1039/TF9625802200>.
- [91] B. Scharifker, G. Hills, Theoretical and experimental studies of multiple nucleation, *Electrochim. Acta* 28 (1983) 879–889, [https://doi.org/10.1016/0013-4686\(83\)85163-9](https://doi.org/10.1016/0013-4686(83)85163-9).
- [92] Z. Yao, X. Fan, L. Kong, Electrochemical deposition of Li<sub>2</sub>S<sub>2</sub>/Li<sub>2</sub>S in aprotic Li-S batteries, *Particology* 90 (2024) 516–521, <https://doi.org/10.1016/J.PARTIC.2024.01.011>.
- [93] G. Di Donato, T. Ates, H. Adenusi, A. Varzi, M.A. Navarra, S. Passerini, Electrolyte measures to prevent polysulfide shuttle in lithium-sulfur batteries, *Batter. Supercaps.* 5 (2022) e202200097, <https://doi.org/10.1002/BATT.202200097>.
- [94] M. Baek, H. Shin, K. Char, J.W. Choi, M. Baek, H. Shin, K. Char, J.W. Choi, New high donor electrolyte for lithium-Sulfur batteries, *Adv. Mater.* 32 (2020) 2005022, <https://doi.org/10.1002/ADMA.202005022>.
- [95] H. Shin, M. Baek, A. Gupta, K. Char, A. Manthiram, J.W. Choi, Recent progress in high donor electrolytes for lithium-Sulfur batteries, *Adv. Energy Mater.* 10 (2020) 2001456, <https://doi.org/10.1002/AENM.202001456>.
- [96] J. Sun, Y. Liu, L. Liu, J. Bi, S. Wang, Z. Du, H. Du, K. Wang, W. Ai, W. Huang, J. Sun, Y. Liu, L. Liu, J. Bi, S. Wang, Z. Du, K. Wang, W. Ai, W. Huang, H. Du, Interface engineering toward expedited Li<sub>2</sub>S deposition in lithium-sulfur

- batteries: a critical review, *Adv. Mater.* 35 (2023) 2211168, <https://doi.org/10.1002/ADMA.202211168>.
- [97] F.Y. Fan, W.C. Carter, Y.M. Chiang, F.Y. Fan, W.C. Carter, Y. Chiang, Mechanism and kinetics of Li<sub>2</sub>S precipitation in lithium–Sulfur batteries, *Adv. Mater.* 27 (2015) 5203–5209, <https://doi.org/10.1002/ADMA.201501559>.
- [98] Z.X. Chen, Y.T. Zhang, C.X. Bi, M. Zhao, R. Zhang, B.Q. Li, J.Q. Huang, Premature deposition of lithium polysulfide in lithium-sulfur batteries, *J. Energy Chem.* 82 (2023) 507–512, <https://doi.org/10.1016/J.JECHEM.2023.03.015>.
- [99] A. Gupta, A. Manthiram, Unifying the clustering kinetics of lithium polysulfides with the nucleation behavior of Li<sub>2</sub>S in lithium–sulfur batteries, *J. Mater. Chem. a Mater.* 9 (2021) 13242–13251, <https://doi.org/10.1039/D1TA02779D>.
- [100] Q. He, B. Yu, H. Wang, M. Rana, X. Liao, Y. Zhao, Oxygen defects boost polysulfides immobilization and catalytic conversion: first-principles computational characterization and experimental design, *Nano Res.* 13 (2020) 2299–2307, <https://doi.org/10.1007/s12274-020-2850-5>.
- [101] X. Huo, Y. Liu, R. Li, J. Li, Two-dimensional Ti<sub>3</sub>C<sub>2</sub>Tx@S as cathode for room temperature sodium-sulfur batteries, *Ionics. (Kiel)* 25 (2019) 5373–5382, <https://doi.org/10.1007/s11581-019-03074-6>.
- [102] J. Yan, X. Liu, B. Li, J. Yan, B. Li, X. Liu, Capacity fade analysis of sulfur cathodes in lithium–sulfur batteries, *Adv. Sci.* 3 (2016) 1600101, <https://doi.org/10.1002/ADVS.201600101>.
- [103] F. Schmidt, S. Ehrling, K. Schönherr, S. Dörfler, T. Abendroth, H. Althues, S. Kaskel, The importance of swelling effects on cathode density and electrochemical performance of lithium–sulfur battery cathodes produced via dry processing, *Energy Technol.* 10 (2022) 2100721, <https://doi.org/10.1002/ENTE.202100721>.